https://doi.org/10.1142/9789811279560_0007

Chapter 7

Quantum Optical Analysis of High-Order Harmonic Generation in Semiconductors

Javier Rivera-Dean[1], Philipp Stammer[1], Andrew S. Maxwell[2], Theocharis Lamprou[3,4], Andrés F. Ordóñez[5], Emilio Pisanty[6], Paraskevas Tzallas[3,7], Maciej Lewenstein[1,8] and Marcelo F. Ciappina[9,10,11]

[1]*ICFO — Institut de Ciencies Fotoniques, The Barcelona Institute of Science and Technology, 08860 Castelldefels (Barcelona), Spain*
[2]*Department of Physics and Astronomy, Aarhus University, DK-8000 Aarhus C, Denmark*
[3]*Foundation for Research and Technology-Hellas, Institute of Electronic Structure & Laser, GR-70013 Heraklion (Crete), Greece*
[4]*Department of Physics, University of Crete, P.O. Box 2208, GR-70013 Heraklion (Crete), Greece*
[5]*Department of Physics, Imperial College London, SW7 2AZ London, United Kingdom*
[6]*Department of Physics, King's College London, WC2R 2LS London, United Kingdom*
[7]*ELI-ALPS, ELI-Hu Non-Profit Ltd., Dugonics tér 13, H-6720 Szeged, Hungary*
[8]*ICREA, Pg. Lluís Companys 23, 08010 Barcelona, Spain*
[9]*Physics Program, Guangdong Technion–Israel Institute of Technology, Shantou, Guangdong 515063, China*
[10]*Technion — Israel Institute of Technology, Haifa, 32000, Israel*
[11]*Guangdong Provincial Key Laboratory of Materials and Technologies for Energy Conversion, Guangdong Technion — Israel Institute of Technology, Shantou, Guangdong 515063, China*

7.1 Introduction

Quantum optics stands as one of the most promising platforms for practical applications in quantum information science, with light serving as the primary carrier of information [1–3]. To advance such applications, non-classical states of light are necessary — states inherently described by quantum electrodynamics tools [4]. Some of the available non-classical light sources rely on nonlinear interactions between light and matter [5], and one of the most striking examples of these interactions is high-order harmonic generation (HHG) [6, 7]. In HHG, a strong, pulsed laser field interacts with matter, resulting in the emission of radiation, emitted as a periodic series of ultrashort harmonics of the driving laser, spanning numerous harmonic orders [8]. While semiclassical theoretical descriptions of HHG processes — where light is treated classically while the matter system is treated quantum mechanically — suffice to replicate most experimental results, they leave untapped the potential of strong-field physics in quantum optics.

Recent years have witnessed renewed attraction in analyzing strong-field processes from a quantum optical perspective [9, 10]. This surge in interest corresponds to the observation of strong laser-matter interactions being useful for creating non-classical states. For example, by means of HHG processes in atomic systems it is possible to generate non-classical states of light [11–16] with intensities enough to drive nonlinear processes in matter [17], as well as massively frequency-entangled states [18, 19], light-matter entangled states [20, 21], and high-photon-number squeezed states [22, 23]. Moreover, it has been demonstrated that the use of non-classical light sources can significantly impact electron dynamics [24–26], resulting in extended and better-resolved harmonic spectra [27], as well as leading to new paradigms regarding the semiclassical interpretation of HHG processes [28, 29].

In this chapter, we delve into recent findings in solid-state systems, specifically semiconductor materials, along these lines where the quantum optical behavior is brought to attention. These systems have been recently analyzed in Ref. [30], demonstrating that the band structure of solids lead to non-trivial effects on the quantum optical state of the system. However, the content presented in this chapter builds upon Refs. [31, 32], which provide a quantum optical description of strongly driven light-matter interactions using two distinct basis sets to characterize the electronic system. Although yielding similar outcomes, these different approaches offer diverse insights

into electron dynamics and provide more suitable frameworks for computing specific quantum information measures.

7.2 Semiclassical Analysis of the Light-Matter Interaction

In this section, we delve into the interaction between a laser field and a solid-state system from a semiclassical perspective. Within this framework, the solid-state system is treated quantum mechanically, while the field is regarded as a linearly polarized classical field. Therefore, under the length gauge and within the dipole approximation, the interaction can be described under a single-active electron picture by the following Hamiltonian

$$\hat{H} = \hat{H}_{\rm cr} + \mathsf{e}\hat{r}_i E_{\rm cl}(t), \tag{7.1}$$

where e denotes the electron charge, $\hat{r}_i$ represents the position operator along the polarization direction $\boldsymbol{\varepsilon}_i$ with i denoting the direction ($i \in \{x, y, z\}$), and $E_{\rm cl}(t)$ stands for a classical electric field. It is worth noting that the dipole approximation is applicable in this context since, as in typical experimental implementations [33, 34], the laser fields used have frequencies within the mid-infrared regime ($\lambda_L \sim$ 1–5 μm), while typical crystal lattices are on the order of 1 Å.

In the expression above, $\hat{H}_{\rm cr}$ denotes the crystal Hamiltonian. We will model this Hamiltonian using a two-band, tight-binding model, with the band-dispersion relations for both the valence (v) and conduction (c) bands satisfying

$$E_v(\mathbf{k}) = \sum_{i=x,y,z} \sum_{j=0}^{\infty} \alpha_{v,i}^{j} \cos(jk_i a_i), \tag{7.2}$$

$$E_c(\mathbf{k}) = E_g + \sum_{i=x,y,z} \sum_{j=0}^{\infty} \alpha_{c,i}^{j} \cos(jk_i a_i), \tag{7.3}$$

where $\mathbf{k}$ denotes the crystal momentum, a_i represents the lattice constant along the i direction, E_g corresponds to the band gap energy at the Γ point, and $\alpha_{m,i}^{j}$ the coefficients arising from expanding the bands within the tight-binding approximation [35].

In the following subsections, we will address the dynamics associated with the Hamiltonian in Eq. (7.1) by employing two basis sets to expand the electronic wavefunctions. First, we adopt a Bloch-based description [36, 37], which are eigenstates of the crystal Hamiltonian and possess a

well-defined crystal momentum. Subsequently, we shift to a Wannier-based description as discussed in Ref. [38] which, in contrast, uses eigenstates localized in space while being entirely delocalized in reciprocal space. Despite the approaches being expected to yield similar results, given that unitary transformations should not impact the physics of the process, they offer distinct insights into the electron dynamics inside the crystal [39].

7.2.1 *Bloch-Bloch Picture*

In this subsection, we focus on a description in which the quantum state of the electron in both the valence and conduction bands is represented using the Bloch basis $\{|\phi_{\mathbf{k},m}\rangle\}$, where m denotes the respective band. As previously mentioned, these states are eigenstates of the crystal Hamiltonian with eigenvalue $E_m(\mathbf{k})$, that is

$$\hat{H}_{\rm cr}\,|\phi_{\mathbf{k},m}\rangle = E_m(\mathbf{k})\,|\phi_{\mathbf{k},m}\rangle, \tag{7.4}$$

while the matrix elements for the corresponding position operator $\hat{r}_i$ have both diagonal and non-diagonal contributions. In the following, we express this operator in terms of its intraband ($\hat{r}_{i,\rm tra}$) and interband ($\hat{r}_{i,\rm ter}$) components, that is

$$\hat{r}_i = \hat{r}_{i,\rm tra} + \hat{r}_{i,\rm ter}. \tag{7.5}$$

As their name suggests, intraband terms involve matrix elements that pertain to Bloch states within the same band, while interband terms relate to Bloch states in different bands. More specifically, we have the following expressions for these matrix elements

$$\langle\phi_{\mathbf{k},m}|\hat{r}_{i,\rm tra}|\phi_{\mathbf{k}',l}\rangle = i\hbar\delta_{m,l}\frac{\partial}{\partial k_i}\delta(\mathbf{k}-\mathbf{k}'), \tag{7.6}$$

$$\langle\phi_{\mathbf{k},m}|\hat{r}_{i,\rm ter}|\phi_{\mathbf{k}',l}\rangle = \frac{1}{\mathsf{e}}d^{(i)}_{ml}(\mathbf{k})\delta(\mathbf{k}-\mathbf{k}'), \tag{7.7}$$

with $d^{(i)}_{ml}(\mathbf{k})$ the dipole moment matrix element between the two bands, which can be generally expressed as [35–37]

$$d^{(i)}_{ml}(\mathbf{k}) = \sqrt{\frac{\mathfrak{E}_{p,i}}{\left[2(E_l(\mathbf{k})-E_c(\mathbf{k}))^2\right]}}, \tag{7.8}$$

where $\mathfrak{E}_{p,i}$ is the so-called Kane parameter, whose values are tabulated for many materials.

In terms of these intraband and interband operators, we can express the Hamiltonian describing the dynamics of this system as

$$i\hbar\frac{\partial\,|\psi(t)\rangle}{\partial t} = \Big[\hat{H}_{\rm cr} + \mathsf{e}\hat{r}_{i,\rm tra}E_{\rm cl}(t) + \mathsf{e}\hat{r}_{i,\rm ter}E_{\rm cl}(t)\Big]\,|\psi(t)\rangle. \tag{7.9}$$

Hereupon, we work in the interaction picture with respect to the intraband excitation component. In more explicit mathematical terms, we introduce in our equations $|\psi(t)\rangle = \hat{U}_{\rm tra}(t)|\bar{\psi}(t)\rangle$. In this expression, $\hat{U}_{\rm tra}(t) = e^{i\mathsf{e}A_{\rm cl}(t)\hat{r}_{i,\rm tra}/\hbar}$ with $A_{\rm cl}(t)$ the classical vector potential related to the electric field via $E_{\rm cl}(t) = -\partial A_{\rm cl}(t)/\partial t$. The rationale behind this transformation arises from the fact that the intraband term, as presented in Eq. (7.6), couples Bloch states with different values of k, leading to a set of coupled differential equations when projecting Eq. (7.9) onto the Bloch basis. By transitioning to the interaction picture with respect to this term, we effectively shift our frame of reference to that of the oscillating electron within the field, and work with the canonical momentum $\mathbf{K} = \mathbf{k} - \mathsf{e}\boldsymbol{\varepsilon_i}A_{\rm cl}(t)$, where $\boldsymbol{\varepsilon_i}$ denotes the polarization direction.

Within this frame, the Schrödinger equation in Eq. (7.9) transforms into

$$i\hbar\frac{\partial|\bar{\psi}(t)\rangle}{\partial t} = \Big[\hat{H}_{\rm cr}(t) + \mathsf{e}\hat{r}_{i,\rm ter}(t)E_{\rm cl}(t)\Big]|\bar{\psi}(t)\rangle, \tag{7.10}$$

where we have defined

$$\hat{H}_{\rm cr}(t) \equiv \hat{U}^{\dagger}_{\rm tra}(t)\hat{H}_{\rm cr}\hat{U}_{\rm tra}(t), \quad \hat{r}_{\rm ter}(t) \equiv \hat{U}^{\dagger}_{\rm tra}(t)\hat{r}_{\rm ter}\hat{U}_{\rm tra}(t), \tag{7.11}$$

and by projecting Eq. (7.10) with respect to the basis set spanned by the canonical crystal momentum $\{|\mathbf{K}, m\rangle\}$, we can rewrite this differential equation as

$$\begin{aligned} i\hbar\frac{\partial b_m(\mathbf{K},t)}{\partial t} &= E_m\big(\mathbf{K} + \mathsf{e}\boldsymbol{\varepsilon}_i A_{\rm cl}(t)\big)b_m(\mathbf{K},t) \\ &\quad + \sum_{l=c,v} d^{(i)}_{ml}\big(\mathbf{K} + \mathsf{e}\boldsymbol{\varepsilon}_i A_{\rm cl}(t)\big)b_l(\mathbf{K},t), \end{aligned} \tag{7.12}$$

defined for both the valence and conduction bands, leading to a set of coupled differential equations. In this expression, the $b_m(\mathbf{K},t) \equiv \big\langle \mathbf{K}\big|\bar{\psi}(t)\big\rangle$ are the probability amplitudes of finding the electron with canonical crystal momentum $\mathbf{K}$ in band m, with $E_m(\mathbf{k})$ the dispersion relation of the mth band, given in Eqs. (7.2) and (7.3).

From this system of differential equations, where as we can see has become uncoupled with respect to $\mathbf{K}$, one can derive what are commonly referred to as semiconductor Bloch equations [39, 40]. These equations

govern the dynamics of the band populations and coherences, denoted here as $n_m(\mathbf{K},t) \equiv b_m^*(\mathbf{K},t)b_m(\mathbf{K},t)$ and $\pi(\mathbf{K},t) \equiv b_v^*(\mathbf{K},t)b_c(\mathbf{K},t)$, respectively. The beneficial aspect about this matrix formulation is that one can straightforwardly include environmental effects into the solid dynamics by adding the corresponding terms affecting either the populations and/or the coherences. Here, we focus on dephasing effects due to electron-electron and electron-phonon couplings, which can be introduced in terms of what is commonly known as a dephasing time T_2 into our equations. With this, the differential equations describing the population and coherence dynamics are given by

$$i\hbar\frac{\partial n_m(\mathbf{K},t)}{\partial t} = \theta_m E_{\rm cl}(t)\big[d_{cv}^{(i)}\big(\mathbf{K}+\mathsf{e}\boldsymbol{\varepsilon}_i A_{\rm cl}(t)\big)\big]^*\pi(\mathbf{K},t) + \text{c.c.}, \tag{7.13}$$

$$i\hbar\frac{\partial \pi(\mathbf{K},t)}{\partial t} = \left[\mathcal{E}_g\big(\mathbf{K}+\mathsf{e}\boldsymbol{\varepsilon}_i A_{\rm cl}(t)\big) + E_{\rm cl}(t)\xi_g^{(i)}\big(\mathbf{K}+\mathsf{e}\boldsymbol{\varepsilon}_i A_{\rm cl}(t)\big) - \frac{i}{T_2}\right] \times \pi(\mathbf{K},t) + E_{\rm cl}(t)d_{cv}^{(i)}(t)\big(\mathbf{K}+\mathsf{e}\boldsymbol{\varepsilon}_i A_{\rm cl}(t)\big)w(\mathbf{K},t), \tag{7.14}$$

where we have defined $\theta_v \equiv 1$ and $\theta_c \equiv -1$, the band gap energy as $\mathcal{E}_g(\mathbf{k}) \equiv E_c(\mathbf{k}) - E_v(\mathbf{k})$, the difference between the Berry connection $d_{mm}^{(i)}(\mathbf{k})$ of each band as $\xi_g^{(i)} \equiv d_{cc}^{(i)}(\mathbf{k}) - d_{vv}^{(i)}(\mathbf{k})$ and the population difference between bands as $w(\mathbf{K},t) \equiv n_v(\mathbf{K},t) - n_c(\mathbf{K},t)$.

These equations allow us to compute one of the most characteristic observables associated to HHG, commonly referred to as the HHG spectrum. This quantity is given as $\omega^2|\text{FT}[j_{i,\text{ter}}(t) + j_{i,\text{tra}}(t)]|^2$, where $j_{i,\text{ter}}(t)$ and $j_{i,\text{tra}}(t)$ represent the time-dependent inter and intraband terms which are, specially for centrosymmetric materials in which the Berry connection is zero [41], the dominant contributions to the HHG process [34, 36, 37, 40] and FT denotes the Fourier transform.

On the one hand, interband dynamics provide an analogous mechanism to the HHG process in atomic and molecular systems, governed by a three step-like model [42–45]. Specifically, for solid-state systems (1) an electron-hole pair is created due to the promotion of the electron to the conduction band, (2) the pair gets accelerated by the field in their respective bands, and (3) the pair meets each other in the valence band by emitting a photon with energy equal to the energy difference between the bands [36, 37]. On the other hand, intraband dynamics provide a mechanism for the emission of radiation related to electron scattering within the energy dispersion profile of the specific band in which it is located. This mechanism is often referred to as Bloch oscillations [46].

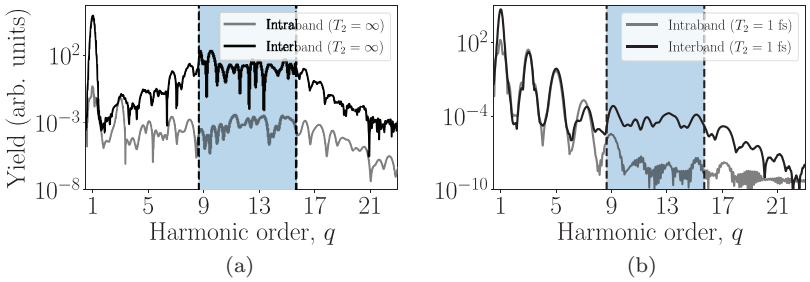

Fig. 7.1 Contributions of interband and intraband currents to the HHG spectra. The spectra have been computed for a ZnO semiconductor after interaction with a linearly polarized field along the $\Gamma - A$ direction, with a peak field strength 0.5 V/Å, central wavelength $\lambda_L = 3.25\,\mu$m and duration of $\Delta t \approx 96$ fs (≈ 9 total cycles). In panel (a), an ideal solid is considered where dephasing effects do not affect the electron dynamics ($T_2 \to \infty$). In contrast, panel (b) considers the case where dephasing effects are indeed included. The dashed blue region span the minimum and maximum energy band gaps for the considered crystal direction.

These current components can be respectively computed from Eqs. (7.13) and (7.14) as

$$j_{i,\mathrm{ter}}(t) = \mathsf{e}\frac{\mathrm{d}}{\mathrm{d}t}\big[\,\mathrm{tr}(\hat{r}_{i,\mathrm{ter}}\hat{\rho}(t))\big], \tag{7.15}$$

$$j_{i,\mathrm{tra}}(t) = -\mathsf{e}\,\mathrm{tr}\Big(\big[\hat{r}_{i,\mathrm{tra}}, \hat{H}_{\mathrm{cr}}\big]\hat{\rho}(t)\big]\Big), \tag{7.16}$$

where $\hat{\rho}(t)$ is the density matrix with populations and coherences given by $n_m(\mathbf{K}, t)$ and $\pi(\mathbf{K}, t)$, when expanded in the canonical crystal momentum basis.

In Fig. 7.1, we present the spectrum calculated for ZnO when excited with a linearly polarized field along the $\Gamma - A$ direction, with field strength 0.5 V/Å, central wavelength $\lambda_L = 3.25\,\mu$m, duration of $\Delta t \approx 96$ fs (≈ 9 total cycles). Specifically, in panel (a) the dephasing time has been set $T_2 \to \infty$, while in panel (b) it is set to $T_2 = 1$ fs. As observed, in both cases, interband contributions dominate over the intraband one within the perturbative part of the spectrum, which is presented in the figure with the blue region delimited by the minimum and maximum energy band gaps for this solid direction. For energies smaller than the minimum energy band gap, i.e., within the perturbative region, no clear dominance is found between them, and the difference becomes less evident for smaller dephasing times. However, dephasing effects have another important consequence, which is that of making the harmonic peaks more evident than in the case

without dephasing ($T_2 \to \infty$). While the use of these small dephasing times to obtain well-resolved theoretical spectra has been common practice in theories describing HHG spectra in solids, their small values have also been a subject of controversy within the attoscience community [47]. And this is mainly because the used values are on the order of a quarter of an optical driving field cycle, while experimental evidence suggest they should be likely on the order of 15∼50 fs at least [48, 49].

In this context, some works justify their values by suggesting that electrons with high values of crystal momentum could decohere at this scales [36]. Others opposing to the presence of these small values propose additional mechanisms beyond electron-photon dephasing. For instance, in Ref. [50], the importance of propagation effects is highlighted in this regard. On the other hand, in Ref. [51], through extensive numerical computations, they observe that issues regarding numerical convergence could potentially be a concern.

7.2.2 *Wannier-Bloch Picture*

Unlike the previous subsection, here we approach the same problem but from a slightly different perspective. Instead of working with Bloch states for both valence and conduction bands, in this subsection, we characterize valence band states using a Wannier basis $\{|w_{j,v}\rangle\}$, with j denoting the Wannier site and v the band. For the conduction band, we utilize Bloch states $\{|\phi_{\mathbf{k},c}\rangle\}$. The main distinction between Wannier and Bloch states is that the former can be defined to be maximally localized in space, while the latter are completely localized in reciprocal space. Thus, this representation in terms of localized states in the valence band provides an atomistic-like interpretation of the HHG process in solids [38]. Specifically, within the single-electron picture, one could understand the electron as initially being localized in a given Wannier site and recombining with a potentially different site, somewhat resembling the localization of an electron in an atomic nucleus.

However, unlike Bloch states, Wannier states are not eigenstates of the crystal Hamiltonian. This highlights an additional degree of freedom electrons have in solid-state systems when compared to atomic ensembles: electrons can hop from one Wannier site to another — a process that does not occur between different atomic nuclei, which are far apart and barely interact with each other. Specifically, the matrix elements of the crystal Hamiltonian under Wannier basis are given, under the tight-binding

approximation, by

$$\langle w_{j,v}|\hat{H}_{\rm cr}|w_{j',v}\rangle = -I_v\delta_{|j-j'|,1}, \tag{7.17}$$

where $I_v < 0$ corresponds to the hopping parameter. This relation implies that we consider only nearest-neighbor interactions between the different sites. However, depending on the specific system that is used, other neighbors may need to be included. It is worth highlighting that, as we are working with linearly polarized fields, in the following we consider a one-dimensional description for the Wannier states such that j is a scalar and not a vector representing the spatial location of the Wannier site in real space.

Initially, the system's state corresponds to a completely filled Fermi sea, indicating that all Wannier states are occupied. However, here we consider a single-active electron description, wherein we solve the equation for a single electron and then combine all results at the end. Thus, under these considerations and in terms of the mixed Wannier-Bloch basis representation, we propose the following ansatz to solve the Schrödinger equation in Eq. (7.9)

$$|\psi(t)\rangle = \sum_j a_j(t)\,|w_{j,v}\rangle + \int \mathrm{d}\mathbf{k} a_c(\mathbf{k},t)\,|\phi_{\mathbf{k},c}\rangle, \tag{7.18}$$

under the initial condition $a_j(0) = \delta_{j,j_0}$. Introducing this ansatz into Eq. (7.9) and projecting it with respect to both a Wannier state $|w_{j,v}\rangle$ and a Bloch state $|\phi_{\mathbf{k},c}\rangle$, we arrive at the following set of coupled differential equations

$$\begin{aligned} i\hbar\frac{\partial a_j(t)}{\partial t} &= -I_v a_{j-1}(t) - I_v a_{j+1}(t) + \mathsf{e} r_j E_{\rm cl}(t) a_j(t) \\ &\quad + E_{\rm cl}(t)\int \mathrm{d}\mathbf{k}\; d_{jc}(\mathbf{k}) a_c(\mathbf{k},t), \end{aligned} \tag{7.19}$$

$$i\hbar\frac{\partial a_c(\mathbf{k},t)}{\partial t} = E_c(\mathbf{k})a_c(\mathbf{k},t) + i\hbar E_{\rm cl}(t)\frac{\partial a_c(\mathbf{k},t)}{\partial k_i} + E_{\rm cl}(t)\sum_j d^*_{jc}(\mathbf{k})a_j(t), \tag{7.20}$$

where r_j represents the position of the jth site, and $d_{jc}(\mathbf{k}) \equiv \mathsf{e}\,\langle w_{j,v}|\,\hat{r}_i\,|\phi_{\mathbf{k},v}\rangle$. This term corresponds to the transition matrix element between an electron in site j of the valence band to a Bloch state with crystal momentum $\mathbf{k}$ in the conduction band.

It is worth noting that the two main dynamics of HHG processes in solids are accounted for in Eqs. (7.19) and (7.20). Specifically, intraband

transitions within the valence band are represented in Eq. (7.19) through the electron hopping between the neighboring sites. Similarly, intraband transition within the conduction band are characterized by the crystal momentum derivatives. Finally, interband transitions between the valence and conduction bands are represented by the terms including the transition dipole matrix elements $d_{jc}(\mathbf{k})$.

For the first equation, and in line with the strong-field approximation (SFA) assumptions [45], we consider the depletion due to conduction band excitations to be very weak in comparison to intraband transitions. Consequently, we approximate Eq. (7.19) as

$$i\hbar\frac{\partial a_j(t)}{\partial t} \approx -I_v a_{j-1}(t) - I_v a_{j+1}(t) + \mathsf{e}r_j E_{\rm cl}(t) a_j(t), \tag{7.21}$$

and perform a discrete Fourier transform over the site label j by multiplying the entire equation by e^{-iqj} and summing over all sites j. Hence, if we define

$$a_q(t) = \sum_j a_j(t) e^{-iqj}, \tag{7.22}$$

the Schrödinger equation in Eq. (7.21) transforms into

$$i\hbar\frac{\partial a_q(t)}{\partial t} = -2I_v \cos(q) a_q(t) + i\hbar\mathsf{e}\mathsf{a}E_{\rm cl}(t)\frac{\partial a_q(t)}{\partial q}, \tag{7.23}$$

with a denoting the lattice constant. This differential equation can also be written as

$$i\hbar\frac{\mathrm{d}a_{\tilde{q}}(t)}{\mathrm{d}t} = -2I_v \cos(\tilde{q} + \mathsf{e}\mathsf{a}E_{\rm cl}(t)) a_{\tilde{q}}(t) \tag{7.24}$$

where $\tilde{q} = q - \mathsf{e}\mathsf{a}A_{\rm cl}(t)$, and whose solution is straightforwardly given by

$$a_{\tilde{q}}(t) = \exp\left[\frac{i}{\hbar} 2I_v \int_{t_0}^{t} \mathrm{d}\tau \cos(\tilde{q} + \mathsf{e}\mathsf{a}A_{\rm cl}(t))\right] a_{\tilde{q}}(t_0). \tag{7.25}$$

Consequently, a solution to Eq. (7.21) can be obtained by inverting the discrete Fourier transform. Thus, we get

$$a_j(t) = \sum_q e^{iq(j-j_0)} \exp\left[\frac{i}{\hbar} 2I_v \int_{t_0}^{t} \mathrm{d}\tau \cos(\tilde{q} + \mathsf{e}\mathsf{a}A_{\rm cl}(t))\right], \tag{7.26}$$

where the initial condition $a_j(t_0) = \delta_{j-j_0}$ has already been implemented.

On the other hand, the solution of Eq. (7.20) is a first-order inhomogeneous differential equation with well-defined homogeneous and

inhomogeneous parts. Hence, its solution can be written as a linear combination of the solution to the homogeneous part and a solution to the inhomogeneous component. In this case, after introducing the initial conditions, we arrive at [38, 52]

$$a_c(\mathbf{K},t) = -\frac{i}{\hbar}\sum_j \int_{t_0}^{t} \mathrm{d}t_1 \exp\left[-\frac{i}{\hbar}\int_{t_0}^{t_1} \mathrm{d}\tau E_c\big(\mathbf{K}+\mathsf{e}\boldsymbol{\varepsilon}_i A_{\mathrm{cl}}(\tau)\big)\right] \times E_{\mathrm{cl}}(t_1) d^*_{jc}\big(\mathbf{K}+\mathsf{e}\boldsymbol{\varepsilon}_i A_{\mathrm{cl}}(t_1)\big) a_j(t_1), \tag{7.27}$$

which bears some resemblance to the atomic ionization process. More specifically, at time t_1 the electron is found at site j, which does not necessarily have to be the initial j_0 according to Eq. (7.26). Then, it undergoes a transition to the conduction band driven by the field at time t_1, represented by the dipole matrix element $d_{jc}(\mathbf{k})$. Finally, it accelerates in the conduction band until time t, with the state gaining an additional phase factor accounting for this process.

Taking into account that [38]

$$d_{jc}(\mathbf{k}) = d_{vc}(\mathbf{k})\tilde{w}_v e^{ikr_j/\hbar}, \tag{7.28}$$

where $\tilde{w}_m$ is a normalization constant for Wannier states which for one-dimensional lattices is k-independent [53], we can write the transition dipole matrix element as

$$\begin{aligned} D(t) =& \ \langle\psi(t)|\hat{r}|\psi(t)\rangle \\ \approx& -\frac{i}{\hbar}|\tilde{w}_v|^2 \sum_{j,j'}\int_{t_0}^{t}\mathrm{d}t_1 \int \mathrm{d}\mathbf{K} a^*_j(t) d_{vc}\big(\mathbf{K}+\mathsf{e}\boldsymbol{\varepsilon}_i A_{\mathrm{cl}}(t)\big) e^{i(\mathbf{K}+\mathsf{e}\boldsymbol{\varepsilon}_i A_{\mathrm{cl}}(t))r_j/\hbar} \\ & \times e^{-i\varphi(p,t,t_1)/\hbar} E_{\mathrm{cl}}(t_1) d^*_{vc}\big(\mathbf{K}+\mathsf{e}\boldsymbol{\varepsilon}_i A_{\mathrm{cl}}(t_1)\big) \\ & + e^{-i(\mathbf{K}+\mathsf{e}\boldsymbol{\varepsilon}_i A_{\mathrm{cl}}(t_1))r_{j'}/\hbar} a_{j'}(t_1) + \mathrm{c.c.}, \end{aligned} \tag{7.29}$$

where we have neglected the contribution of intraband transitions with the aim of accounting only for the dominant interband transitions in the non-perturbative part of the HHG spectrum. In this expression, we have further defined $\varphi(p,t,t_1) \equiv \int_{t_1}^{t} \mathrm{d}\tau E_c(\mathbf{K}+\mathsf{e}\boldsymbol{E}_i A_{\mathrm{cl}}(\tau))$. This time-dependent dipole moment, whose Fourier transform leads to the HHG spectrum, yields similar dynamics to those occurring in atomic systems. First, at time t_1 the electron gets ionized from the Wannier site j' to the conduction band. Within the conduction band, it accelerates gaining a phase $\varphi(p,t,t_1)$, and recombines at time t with the jth site.

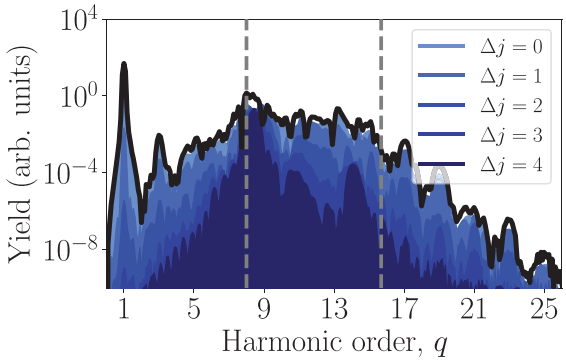

Fig. 7.2 The interband contribution to the HHG spectrum, following the Wannier-Bloch approach presented in the text, is computed for a ZnO material that has been excited with a linearly polarized field along the $\Gamma - A$ direction. In this case, the field strength considered is $E_0 \approx 0.2\,\mathrm{V/Å}$, central wavelength $\lambda_L = 3.0\,\mu\mathrm{m}$, and duration $\Delta t \approx 100\,\mathrm{fs}$ (≈ 10 optical cycles). The different colors represent the different contributions to the spectra depending on the distance between the initial and final Wannier sites. The black curve represents the total contribution. This figure is based on Fig. 3 in Ref. [38].

Given that in general $j \neq j'$, one can already observe one of the main distinctions between HHG in atoms and solid-state systems. While for atoms the electron performs closed trajectories, meaning that ionization and recombination take place at the same real-space position, for solids this is not necessarily the case. This could be a potential explanation for the reduced dependence of harmonic generation on the field's ellipticity found in solid systems [34]. However, depending on the material considered and how the excitation process takes place (for instance, the crystal direction along which the laser is polarized), the influence of increasing values $\Delta j = |j - j'|$ on the HHG spectra might differ. In Fig. 7.2, this is shown for a ZnO material excited by a linearly polarized field parallel to the $\Gamma - A$ direction, with field strength $E_0 \approx 0.2\,\mathrm{V/Å}$, central wavelength $\lambda_L = 3.0\,\mu\mathrm{m}$ and duration of $\Delta t \approx 100\,\mathrm{fs}$ (≈ 10 optical cycles). As observed, in this case, the contribution to the HHG spectra starts to decay already for $\Delta j \geq 2$, meaning that for this particular case, the HHG process is highly localized.

It is worth noting that the HHG spectra obtained here recovers the characteristic features shown in Fig. 7.1 (a) (black curve), with a plateau structure defined within the lowest and maximum values of the energetic band gap. Furthermore, in this figure we also observe that the absence of dephasing effects leads to poorly resolved harmonic peaks. In this direction,

it has been recently observed in Ref. [54] that the destructive interference of long trajectories, i.e., those with Δj being large, recovers well-resolved harmonic peaks without having to resort to extremely small dephasing times. Similar to atomic systems, this destructive interference could be related to additional phase factors depending on the intensity profile of the applied laser field.

7.3 Quantum Optical Analysis of the Light-Matter Interaction

The discussion thus far on the interaction between strong laser fields and solid-state systems has remained at a semiclassical level: the solid-state system has been studied under a quantum mechanical framework while light has been treated as a classical field. However, as mentioned in the Introduction, delving into the quantum optical regime enables the exploration of concepts such as non-classical light and light-matter entanglement, broadening the spectrum of degrees of freedom in strong-field physics. In the following subsections, after briefly introducing the fundamentals of quantum optics, we expand the previously presented semiclassical analysis to the quantum optical context, drawing from Refs. [31, 32]. We illustrate how the various electron dynamics within the solid affect the joint state of the system following the interaction between light and solid.

7.3.1 *A Brief Introduction to Quantum Optics*

Quantum optics explores the properties of light and its interaction with matter under a quantum mechanical perspective. As the aim of this chapter is to delineate the interaction between light and matter considering the quantum mechanical nature of light, we provide an overview of fundamental concepts and tools within quantum optics for clarity and contextual understanding.

The foundations of quantum optics rely on the realization that the energy associated with an electromagnetic field in free space can be represented as a collection of uncoupled harmonic oscillators (see, e.g., Refs. [55–58] and references therein). Within this assembly, each electromagnetic field mode, characterized by a wavevector $\boldsymbol{k}$ and a polarization μ, corresponds to an oscillator. The Hamiltonian operator associated to this oscillator is characterized by

$$\hat{H}_{\mathbf{k},\mu} = \frac{1}{2}\left[\hat{p}_{\boldsymbol{k},\mu} + \omega_k^2 \hat{x}^2_{\boldsymbol{k},\mu}\right], \tag{7.30}$$

where $\hat{p}_{\boldsymbol{k},\mu}$ and $\hat{x}_{\boldsymbol{k},\mu}$ are the canonical operators of the harmonic oscillator, satisfying the set of commutation relations

$$[\hat{x}_{\boldsymbol{k},\mu}, \hat{p}_{\boldsymbol{k},\mu}] = i\hbar, \quad \left[\hat{x}_{\boldsymbol{k},\mu}, \hat{x}'_{\boldsymbol{k}',\mu}\right] = \left[\hat{p}_{\boldsymbol{k},\mu}, \hat{p}'_{\boldsymbol{k}',\mu}\right] = 0. \tag{7.31}$$

The Hamiltonian introduced in Eq. (7.30) corresponds to a single harmonic oscillator. Hence, for the entire electromagnetic field the Hamiltonian is constructed as a linear combination of these individual oscillators, i.e., $\hat{H}_{\text{field}} = \sum_{\boldsymbol{k},\mu} \hat{H}_{\boldsymbol{k},\mu}$. However, for simplicity in the subsequent discussion within this section, we focus solely on a single electromagnetic field mode $(\boldsymbol{k}, \mu)$. Consequently, we omit the $(\boldsymbol{k}, \mu)$ sub-indexes when referring to the operators to enhance clarity. Furthermore, we introduce a set of creation and annihilation operators, denoted as $\hat{a}^\dagger$ and $\hat{a}$ respectively, linked to the canonical variables $\hat{x}$ and $\hat{p}$ by the following canonical transformations

$$\hat{x} = \sqrt{\frac{\hbar}{2\omega}}\left[\hat{a}^\dagger + \hat{a}\right], \quad \hat{p} = i\sqrt{\frac{\hbar\omega}{2}}\left[\hat{a}^\dagger - \hat{a}\right], \tag{7.32}$$

which satisfy the following set of commutation relations

$$\left[\hat{a}, \hat{a}^\dagger\right] = 1, \quad [\hat{a}, \hat{a}] = \left[\hat{a}^\dagger, \hat{a}^\dagger\right] = 0. \tag{7.33}$$

According to these, the Hamiltonian in Eq. (7.30) can be rewritten as

$$\hat{H} = \hbar\omega\left(\hat{a}^\dagger\hat{a} + \frac{1}{2}\right), \tag{7.34}$$

which is diagonalized by the set of Fock states $\{|n\rangle : n \in \mathbb{W}\}$[1] with corresponding eigenvalues $\{\hbar\omega(n + 1/2) : n \in \mathbb{W}\}$. These states are often referred to as *photon-number* states, with $|n = 0\rangle$ usually denoted as the *vacuum* state, and they represent the discrete excitations of the electromagnetic field. The action of the creation and annihilation operators over these states is expressed as

$$\hat{a}\,|n\rangle = \sqrt{n}\,|n-1\rangle\,, \quad \hat{a}^\dagger\,|n\rangle = \sqrt{n+1}\,|n+1\rangle, \tag{7.35}$$

which respectively destroy and create an electromagnetic field excitation.

In this quantum optical context, the classical electric field $\mathbf{E}_{\text{cl}}(t)$ and vector potential $\mathbf{A}_{\text{cl}}(t)$ are substituted with the quantum mechanical

[1]Here, $\mathbb{W}$ represents the set of whole numbers, i.e., the natural numbers including zero.

operators $\hat{\mathbf{A}}(t)$ and $\hat{\mathbf{E}}(t)$. The single-mode components of these operators are given by

$$\hat{A}(t) = \sqrt{\frac{\hbar}{2\omega\varepsilon_0 V}}\left[\hat{a}e^{-i\omega t} + \hat{a}^\dagger e^{i\omega t}\right] \tag{7.36}$$

$$\hat{E}(t) = i\sqrt{\frac{\hbar\omega}{2\varepsilon_0 V}}\left[\hat{a}e^{-i\omega t} - \hat{a}^\dagger e^{i\omega t}\right], \tag{7.37}$$

where ε_0 represents the vacuum permittivity and V stands for the quantization volume arising when expanding the electromagnetic field in terms of discrete modes. Specifically, for Fock states, we get $\langle n|\hat{E}(t)|n\rangle = 0$ $\forall n \in \mathbb{W}$, while their variance scales proportionally with the number of photons n, i.e., $\Delta E^2(t) = (\hbar\omega)/(2\varepsilon_0 V)[2n+1]$. Moreover, when examining the uncertainty product between the quadrature operators $\hat{x}$ and $\hat{p}$, which are conjugate variables, it is observed that $\Delta x \Delta p = (\hbar/2)(2n+1)$, generally exceeding Heinseberg's uncertainty limit of $\hbar/2$. Consequently, Fock states do not offer an optimal description of classical descriptions of light, as they generally fail to reach this uncertainty product.

In this context, coherent states [59,60] of light reintroduce the notion of a classically oscillating field that provides a solution to Maxwell's equations in vacuum. The coherent states, denoted as $\{|\alpha\rangle : \alpha \in \mathbb{C}\}$, are described as displaced vacuum states, that is

$$|\alpha\rangle = \hat{D}(\alpha)\,|0\rangle, \tag{7.38}$$

where $\hat{D}(\alpha) \equiv \exp\left[\alpha\hat{a}^\dagger - \alpha^*\hat{a}\right]$ represents the displacement operator. From this definition, and using the displacement operator properties, it follows that coherent states are eigenstates of the creation operator, that is,

$$\hat{a}\,|\alpha\rangle = \alpha\,|\alpha\rangle. \tag{7.39}$$

This last property of coherent states becomes particularly useful when evaluating the mean value of the electric field operator

$$\langle\alpha|\hat{E}(t)|\alpha\rangle = \sqrt{\frac{2\hbar\omega}{\epsilon_0 V}}|\alpha|\sin(\omega t - \theta), \tag{7.40}$$

where we have written $\alpha = |\alpha|e^{i\theta}$. Thus, coherent states of light indeed restore the oscillating nature of the electric field and result in a variance of this operator independent of the number of photons $\langle n\rangle = |\alpha|^2$. Specifically, we obtain $\Delta E^2 = (\hbar\omega)/(2\varepsilon_0 V)$. This behavior arises from coherent states providing an optimal description for the classical description

of light, as they saturate the product between the quadrature operators' variance, i.e., $\Delta x \Delta p = (\hbar/\omega)$. This, among other reasons [61], justifies our previous statement: that these states recover a classical description of light. Therefore, we refer to *non-classical* states of light as those states exhibiting features unaccounted for by classical optics theories, Fock states being a particular example.

In general, distinguishing between classical and non-classical states of light often relies on the definition of specific observables. One of the most crucial, although not the sole determinant, is the Wigner function [62, 63], which captures all the information about a quantum state in phase space. Initially proposed in the context of quantum corrections to thermodynamic equilibrum [62], it has found widespread use in quantum optics as an indicator of non-classical states of light [64, 65] by featuring negative values in certain phase space regions. Nonetheless, it is essential to note that the absence of negative values in this function does not inherently imply the *classicality* of the state. Other indicators of non-classical behavior, like sub-Poissonian statistics, might manifest in states characterized by positive-valued Wigner functions.

The Wigner function of a given quantum state $\hat{\rho}$ can be computed as [66]

$$W(\beta) = \mathrm{tr}\Big[\hat{\rho}\hat{D}(\beta)\hat{\Pi}\hat{D}(-\beta)\Big], \tag{7.41}$$

where $\hat{\Pi}$ denotes the parity operator, and β a parameter related to the optical quadratures through $x \equiv \mathrm{Re}(\beta)$ and $p \equiv \mathrm{Im}(\beta)$. In Fig. 7.3, we present examples of different light states displaying different Wigner functions. In panel (a), a coherent state with amplitude $\alpha = 0$ is shown, i.e., a vacuum state. These states feature Gaussian Wigner functions without

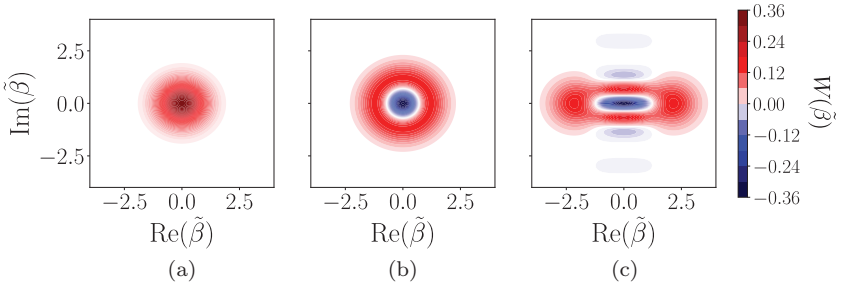

Fig. 7.3 Wigner functions of different states. (a) A vacuum state represented by a coherent state with $|\alpha| = 0$. (b) Wigner function for a Fock state $|n = 1\rangle$. (c) Wigner function of a coherent state superposition $|\alpha\rangle - |-\alpha\rangle$, with $|\alpha| = 1.5$.

negative regions. Conversely, Fock states with $n > 0$ exhibit Wigner functions containing negative regions, as shown in panel (b) for $|n = 1\rangle$. Interestingly, while coherent states themselves lack negative Wigner values in phase space, this is not necessarily true for superpositions composed by different coherent states, i.e., $|\Phi\rangle = \sum_{i=1}^{N} a_i |\alpha_i\rangle$, with $N \geq 2$ and $\alpha_i \neq \alpha_j$ $\forall i \neq j$. In panel (c), we illustrate the case of a coherent state superposition $|\Phi\rangle \propto |\alpha\rangle - |-\alpha\rangle$ with $\alpha = 1.5$. In this instance, quantum interference between the two terms in the superposition, represented by the two maxima at $\mathrm{Re}(\beta) \approx \pm 1.5$, leads to negative regions between these maxima within the Wigner function.

While the Wigner function can indicate non-classical aspects in individual modes of light, in many other situations we have systems composed by multiple subsystems, forming a composite Hilbert space denoted as $\mathcal{H}_T = \bigotimes_{i=1}^{N_\mathrm{s}} \mathcal{H}_i$, where N_s represents the number of subsystems. In optics, these Hilbert spaces often represent various modes of light, such as different polarization and/or frequency modes. In this broader context, states $|\psi\rangle \in \mathcal{H}_T$ may exhibit non-classical features beyond the mere presence of negative regions in their Wigner functions. A notable example is the concept of *entanglement*, which pertains to certain quantum states that cannot be expressed as the tensor product of their individual components [67], that is

$$|\psi\rangle \text{ is entangled if } |\psi\rangle \neq \bigotimes_{i=1}^{N_\mathrm{s}} |\psi_{\mathcal{H}_i}\rangle, \tag{7.42}$$

where $|\psi_{\mathcal{H}_i}\rangle \in \mathcal{H}_i$.

Determining whether a given state $\hat{\rho}$ is entangled is a problem known to be NP-hard[2] [68]. However, in certain scenarios, such as for bipartite systems involving only two subsystems, it is possible to define mathematical functions that offer a quantitative assessment of entanglement. These functions are commonly known as entanglement measures. Among these measures, one of the most prominent is the von Neumann entropy [69], also referred to as entanglement entropy [70]. For a pure state $|\psi_{AB}\rangle \in \mathcal{H}_A \otimes \mathcal{H}_B$, this quantity is defined as

$$\mathcal{S}(\hat{\rho}) := -\,\mathrm{tr}[\hat{\rho}_A \log_d(\hat{\rho}_A)], \tag{7.43}$$

[2]Nondeterministic polynomial (NP) problems comprise decision problems for which instances with affirmative answers can have their proofs verified in polynomial time. NP-hard problems, in this context, are as challenging as NP problems but may not necessarily belong to NP.

where $\hat{\rho}_A$ is the reduced density of $|\psi_{AB}\rangle$ with respect to subsystem B, defined as $\hat{\rho}_A \equiv \mathrm{tr}_B(|\psi_{AB}\rangle\langle\psi_{AB}|)$. In this expression, d represents the dimension of $\mathcal{H}_A$. Notably, although in this expression we have focused on subsystem A, the usage of A and B can be interchanged. If our quantum state is separable, i.e., $|\psi_{AB}\rangle = |\psi_A\rangle \otimes |\psi_B\rangle$, then it can be proven that $\mathcal{S}(\hat{\rho}) = 0$, indicating no entanglement. Conversely, states where $\mathcal{S}(\hat{\rho}) = 1$ are termed maximally entangled. Utilizing entangled states, particularly maximally entangled ones, forms the cornerstone of quantum information science applications such as quantum communication [71, 72] and quantum computation [73, 74], among others [75].

However, in numerous scenarios, both Hilbert spaces $\mathcal{H}_A$ and $\mathcal{H}_B$ can have exceedingly large dimensions. Evaluating the entanglement entropy in Eq. (7.43) under these circumstances becomes numerically challenging, prompting the search for more computationally tractable alternatives. One such example is the linear entropy, defined as

$$\mathcal{S}_{\mathrm{lin}}(\hat{\rho}) := 1 - \mathrm{tr}\big(\hat{\rho}_A^2\big), \tag{7.44}$$

where $\hat{\rho}_A^2$ is termed the purity of the state $\hat{\rho}_A$. The linear entropy corresponds to a second-order expansion of the von Neumann entropy in terms of $\hat{\rho}_A$, and akin to the latter, it becomes zero for separable states. In contrast, its maximum value is bounded by $1 - (1/d)$.

In Fig. 7.4, we present both entanglement measures evaluated on a generic two-qubit state of the form $|\Psi_{AB}\rangle = \sqrt{p}\,|0_A\rangle \otimes |0_B\rangle + \sqrt{1-p}\,|1_A\rangle \otimes |1_B\rangle$ as a function of p. For $p = 0$ and $p = 1$, corresponding to a separable state, both entanglement measures tend to zero. Conversely, the maximum value for both functions occurs at $p = 0.5$, representing a maximally entangled state $|\psi_{AB}\rangle \propto |0_A\rangle \otimes |0_B\rangle + |1_A\rangle \otimes |1_B\rangle$. The use of these entanglement measures, along with the Wigner function, will be of fundamental interest in the subsequent sections of this chapter.

7.3.2 *Bloch-Bloch Picture*

With all the fundamental quantum optics concepts set, let us delve into a quantum optical treatment of the interaction between a solid-state system and a strong laser field, based on an expansion of the electronic states in the Bloch basis. Specifically, we built upon the analysis provided in Sec. 7.2.1 by including in the Hamiltonian presented in Eq. (7.1) the electric field operator. In this context, the Hamiltonian reads

$$\hat{H}(t) = \hat{H}_{\mathrm{cr}} + \mathsf{e}\hat{r}_{i,\mathrm{tra}}\hat{E}(t) + \mathsf{e}\hat{r}_{i,\mathrm{ter}}\hat{E}(t) + \hat{H}_{\mathrm{field}}, \tag{7.45}$$

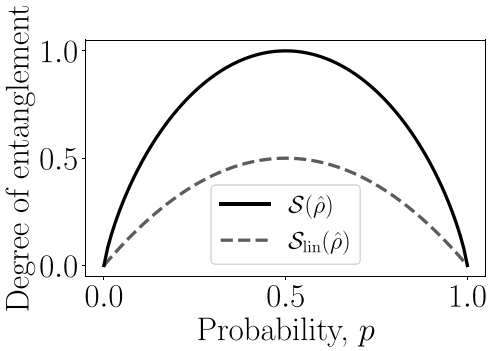

Fig. 7.4 Entanglement measures evaluated for a state in the form $\sqrt{p}\,|0_A\rangle \otimes |0_B\rangle + \sqrt{1-p}\,|1_A\rangle \otimes |1_B\rangle$ plotted as functions of p. The black solid curve represents the entanglement entropy, while the grey dashed curve represents the linear entropy. As expected, both measures tend toward zero when the state becomes separable ($p = 0$ and $p = 1$), and they reach a maximum at $p = 0.5$ corresponding to a maximally entangled state.

where $\hat{H}_{\text{field}}$ represents the free-field Hamiltonian and $\hat{E}(t)$ the electric field operator. Our objective is to characterize interactions with lasers of finite duration, which ultimately necessitates the inclusion of a continuum spectrum of light [13]. However, for simplicity, we limit ourselves to a discrete set of modes spanning the harmonic modes from the central frequency of the employed pulse, ω_L, up to the cutoff region of the harmonic spectrum, $\omega_{q_c} = q_c\omega_L$. Thus, we represent the free-field Hamiltonian as $\hat{H}_{\text{field}} \equiv \sum_{q=1}^{q_c} \hbar\omega_q \hat{a}_q^\dagger \hat{a}_q$ where $\omega_q = q\omega_L$ ($\omega_{q=1} \equiv \omega_L$) and $\hat{a}_q^\dagger$ ($\hat{a}_q$) is the creation (annihilation) operator acting on the field mode of frequency q. The electric field operator is similarly expressed as

$$\hat{E}(t) = if(t) \sum_{q}^{q_c} \mathrm{g}(\omega_q)\big(\hat{a}_q - \hat{a}_q^\dagger\big), \tag{7.46}$$

where $\mathrm{g}(\omega_q) \equiv \sqrt{\hbar\omega_q/(2\varepsilon_0 V)}$ and $0 \leq f(t) \leq 1$ is a dimensionless function accounting for the pulse envelope.

Within this approximation of considering a discrete set of modes, we can represent the initial state of the system composed by

$$|\Psi(t = t_0)\rangle = |\phi_{\mathbf{k}_0,v}\rangle \otimes |\alpha_L\rangle \bigotimes_{q=2}^{q_c} |0_q\rangle, \tag{7.47}$$

such that the single-active electron is initially in the valence band with crystal momentum $\mathbf{k}_0$, while the driving field mode is in a coherent state

α_L with amplitudes on the order of 10^5. Meanwhile, as all harmonic modes begin in an unoccupied state, they are initialized as vacuum states. The overall system dynamics are described by the Schrödinger equation

$$i\hbar\frac{\partial\,|\Psi(t)\rangle}{\partial t} = \big[\hat{H}_{\rm cr} + \mathsf{e}\hat{r}_{i,\rm tra}\hat{E}(t) + \mathsf{e}\hat{r}_{i,\rm ter}\hat{E}(t) + \hat{H}_{\rm field}\big], \tag{7.48}$$

although the analysis can be further simplified by introducing some unitary transformations. Thus, using

$$|\Psi(t)\rangle = \hat{D}_1(\alpha_L)e^{-i\hat{H}_{\rm field}t/\hbar}\left|\tilde{\Psi}(t)\right\rangle, \tag{7.49}$$

the differential equation in Eq. (7.48) can be rewritten as

$$\begin{aligned} i\hbar\frac{\partial|\tilde{\Psi}(t)\rangle}{\partial t} = \big[\hat{H}_{\rm cr} &+ \mathsf{e}\hat{r}_{i,\rm tra}\big(E_{\rm cl}(t) + \hat{E}(t)\big) \\ &+ \mathsf{e}\hat{r}_{i,\rm ter}\big(E_{\rm cl}(t) + \hat{E}(t)\big)\big]|\tilde{\Psi}(t)\rangle, \end{aligned} \tag{7.50}$$

where $E_{\rm cl}(t) = {\rm tr}(\hat{E}(t)\,|\Psi(t_0)\rangle\langle\Psi(t_0)|)$. These transformations introduce an extra time dependence on the electric field operator, effectively shifting us to the interaction picture with respect to $\hat{H}_{\rm field}$

$$\hat{E}(t) = if(t)\sum_q^{q_c}{\rm g}(\omega_q)\big(\hat{a}_q e^{-i\omega_q t} - \hat{a}_q^\dagger e^{i\omega_q t}\big), \tag{7.51}$$

and displaces the origin of our frame of reference in phase space onto the coherent state $|\alpha_L\rangle$, thus leading to the following initial state for this equation

$$|\tilde{\Psi}(t)\rangle = |\phi_{\mathbf{k}_0,v}\rangle\bigotimes_{q=1}^{q_c}|0_q\rangle. \tag{7.52}$$

The transformations we have outlined are customary in the quantum optical analysis of HHG processes in atomic [11–13, 15] and molecular [21] systems. When examining solid-state targets, along the same lines to what is done in the semiclassical analysis, we introduce an additional transformation akin to the $\hat{U}_{\rm tra}(t)$ performed in Sec. 7.2.1. Specifically, we consider

$$|\tilde{\Psi}(t)\rangle = e^{i(\mathsf{e}A_{\rm cl}(t)+\hat{A}(t))\hat{r}_{i,\rm tra}/\hbar}|\bar{\Psi}(t)\rangle, \tag{7.53}$$

with $\hat{A}(t)$ satisfying $\hat{E}(t) = -\,\partial\hat{A}(t)\big/\partial t$. By substituting this expression into Eq. (7.50) and considering terms up to first order in ${\rm g}(\omega_q) \sim 10^{-8}$ a.u., which weighs the quantum optical fluctuations, we can approximate

our differential equation as

$$i\hbar\frac{\partial|\bar{\Psi}(t)\rangle}{\partial t} \approx \big[\hat{H}_{\rm cr}(t) + \mathsf{e}\hat{r}_{i,\rm ter}(t)\big(E_{\rm cl}(t) + \hat{E}(t)\big) - i\mathsf{e}\hbar^{-1}\hat{v}_{i,\rm tra}(t)\hat{A}(t)\big]|\bar{\Psi}(t)\rangle, \tag{7.54}$$

where $\hat{v}_{i,\rm tra} \equiv [\hat{r}_{i,\rm tra}, \hat{H}_{\rm cr}]$. Additionally, the extra time-dependent terms observed in the operators acting on the electron resemble those outlined in Eq. (7.11). Furthermore, these expressions have been derived assuming that inter- and intraband terms are the primary contributors to the HHG in solids. Yet, other factors like the mixture current, whose effects are not fully comprehended from the semiclassical perspective [40], are not considered in this analysis.

The reason for introducing these transformations lies in Eq. (7.54), where the first two terms describe the semiclassical evolution detailed in Sec. 7.2.1. Having solved for these terms as presented in previous subsections, we introduce an additional unitary transformation $|\tilde{\Psi}(t)\rangle = \hat{U}_{\rm sc}(t,t_0)|\tilde{\Psi}'(t)\rangle$ with $\hat{U}_{\rm sc}(t,t_0) \equiv \hat{\mathcal{T}}\exp\Big[-i\int_{t_0}^{t}\mathrm{d}\tau\hat{\bar{H}}_{\rm sc}(\tau)/\hbar\Big]$, accounting for the semiclassical dynamics. Here, $\hat{\mathcal{T}}$ denotes the time-ordering operator, and $\hat{\bar{H}}_{\rm sc}(\tau) \equiv \hat{H}_{\rm cr}(t) + \mathsf{e}\hat{r}_{i,\rm ter}(t)E_{\rm cl}(t)$. As a result, our Schrödinger equation transforms into

$$i\hbar\frac{\partial|\tilde{\Psi}'(t)\rangle}{\partial t} \approx \big[\mathsf{e}\hat{\tilde{r}}_{i,\rm ter}(t)\hat{E}(t) - i\mathsf{e}\hbar^{-1}\hat{\tilde{v}}_{i,\rm tra}(t)\hat{A}(t)\big]|\tilde{\Psi}'(t)\rangle, \tag{7.55}$$

where $\hat{\tilde{r}}_{i,\rm ter} \equiv \hat{U}_{\rm sc}^{\dagger}(t,t_0)\hat{r}_{i,\rm ter}(t)\hat{U}_{\rm sc}(t,t_0)$ and $\hat{\tilde{v}}_{i,\rm tra} \equiv \hat{U}_{\rm sc}^{\dagger}(t,t_0)\hat{v}_{i,\rm tra}(t)\hat{U}_{\rm sc}(t,t_0)$.

With the aim of solving this differential equation, we expand our state in the $\{|\mathbf{K},m\rangle\}$ basis, that is

$$|\tilde{\Psi}'(t)\rangle = \sum_{m=v,c}\int \mathrm{d}\mathbf{K}\,|\mathbf{K},m\rangle \otimes |\Phi_m(\mathbf{K},t)\rangle, \tag{7.56}$$

where $|\Phi_m(\mathbf{K},t)\rangle = \langle\mathbf{K},m|\tilde{\Psi}'(t)\rangle$ corresponds to the quantum optical state conditioned on finding an electron in band m and with canonical crystal momentum $\mathbf{K}$. Introducing this expression into Eq. (7.55) and projecting the whole equation with respect to $|\mathbf{K},m\rangle$, we arrive at

$$i\hbar\frac{\partial}{\partial t}|\Phi_m(\mathbf{K},t)\rangle = \sum_{l=c,v}\int \mathrm{d}\mathbf{K}'\big[\mathsf{e}\,\langle\mathbf{K},m|\,\hat{\tilde{r}}_{i,\rm ter}(t)\,|\mathbf{K}',l\rangle\,\hat{E}(t) - i\mathsf{e}\hbar^{-1}\,\langle\mathbf{K},m|\,\hat{\tilde{v}}_{i,\rm tra}(t)\,|\mathbf{K}',l\rangle\,\hat{A}(t)\big]. \tag{7.57}$$

In order to further proceed in solving the set of differential equations spanned by Eq. (7.57), it is necessary to evaluate the electronic matrix elements appearing in the above expressions. By taking into account the semiclassical evolution described in Eq. (7.12), which leads us to

$$\hat{U}_{\rm sc}(t,t_0)\,|\mathbf{K},m\rangle = b_v(\mathbf{K},t;m)\,|\mathbf{K},v\rangle + b_c(\mathbf{K},t;m)\,|\mathbf{K},c\rangle, \tag{7.58}$$

and after some algebraic operations, it is possible to show that

$$\begin{aligned}
&\int \mathrm{d}\mathbf{K}'\,\langle \mathbf{K},m|\,\hat{\bar{r}}_{i,\rm ter}(t)\,|\mathbf{K}',l\rangle\,|\mathbf{K}',l\rangle \\
&\quad = \sum_{\mathsf{i}=v,c}\sum_{\mathsf{j}=v,c} b^*_{\mathsf{i}}(\mathbf{K},t;m)b^*_{\mathsf{j}}(\mathbf{K},t;l)d_{\mathsf{ij}}\big(\mathbf{K}+\mathsf{e}\boldsymbol{\varepsilon}_i A_{\rm cl}(t)\big)\,|\mathbf{K},l\rangle \\
&\quad \equiv \mathsf{e}^{-1}M^{(\rm ter)}_{m,l}\,|\mathbf{K},l\rangle,
\end{aligned} \tag{7.59}$$

while for the other term we get

$$\begin{aligned}
&\int \mathrm{d}\mathbf{K}'\,\langle \mathbf{K},m|\,\hat{\bar{v}}_{i,\rm tra}(t)\,|\mathbf{K}',l\rangle\,|\mathbf{K}',l\rangle \\
&\quad = i\hbar\sum_{\mathsf{i}=v,c} b^*_{\mathsf{i}}(\mathbf{K},t;m)b_{\mathsf{i}}(\mathbf{K},t;l)\frac{\partial}{\partial K_i}\big[E_{\mathsf{i}}\big(\mathbf{K}+\mathsf{e}\boldsymbol{\varepsilon}_i A_{\rm cl}(t)\big)\big]\,|\Phi_l(\mathbf{K},t)\rangle \\
&\quad \equiv i\mathsf{e}^{-1}\hbar M^{(\rm tra)}_{m,l}(\mathbf{K},t)\,|\Phi_l(\mathbf{K},t)\rangle.
\end{aligned} \tag{7.60}$$

These expressions we have just presented are associated with the inter- and intraband currents delineated in Eqs. (7.15) and (7.16). The former corresponds to the time-dependent interband polarization, while the latter deals with the intraband current. However, the quantum optical treatment conducted here has been performed under a noiseless scenario, lacking explicit inclusion of dephasing effects. Nonetheless, these could be incorporated when evaluating the matrix elements $M^{(\rm ter)}_{m,l}(\mathbf{K},t)$ and $M^{(\rm tra)}_{m,l}(\mathbf{K},t)$. It is important to note that this approach is akin to describing the crystal using non-Hermitian Hamiltonians. Similar strategies have been employed in semiclassical analyses [76], yielding analogous outcomes to those presented in Sec. 7.2.1.

Introducing Eqs. (7.15) and (7.16) into Eq. (7.57), and explicitly distinguishing between projections on valence and conduction bands, we obtain the following set of coupled differential equations

$$\begin{aligned}
i\hbar\frac{\partial}{\partial t}\,|\Phi_v(\mathbf{K},t)\rangle = &\big[M^{(\rm ter)}_{v,v}(\mathbf{K},t)\hat{E}(t) + M^{(\rm tra)}_{v,v}\hat{A}(t)\big]\,|\Phi_v(\mathbf{K},t)\rangle \\
&+ \big[M^{(\rm ter)}_{v,c}(\mathbf{K},t)\hat{E}(t) + M^{(\rm tra)}_{v,c}\hat{A}(t)\big]\,|\Phi_c(\mathbf{K},t)\rangle,
\end{aligned} \tag{7.61}$$

$$i\hbar\frac{\partial}{\partial t}\left|\Phi_c(\mathbf{K},t)\right\rangle = \left[M_{c,v}^{(\mathrm{ter})}(\mathbf{K},t)\hat{E}(t) + M_{c,v}^{(\mathrm{tra})}\hat{A}(t)\right]\left|\Phi_v(\mathbf{K},t)\right\rangle + \left[M_{c,c}^{(\mathrm{ter})}(\mathbf{K},t)\hat{E}(t) + M_{c,c}^{(\mathrm{tra})}\hat{A}(t)\right]\left|\Phi_c(\mathbf{K},t)\right\rangle, \quad (7.62)$$

where each of the equations have both a homogeneous and an inhomogeneous component. Thus, their solution can be expressed as the sum of the solution to the homogeneous equation plus a particular solution to the inhomogeneous one. Let us start by the former, for which we have

$$i\hbar\frac{\partial}{\partial t}\left|\Phi_{\mathrm{i,hom}}(\mathbf{K},t)\right\rangle = \left[M_{\mathrm{i,i}}^{(\mathrm{ter})}(\mathbf{K},t)\hat{E}(t) + M_{\mathrm{i,i}}^{(\mathrm{tra})}\hat{A}(t)\right]\left|\Phi_{\mathrm{i,hom}}(\mathbf{K},t)\right\rangle, \quad (7.63)$$

and taking into account the definitions we consider in a discrete mode description for the electric field and vector potential operators

$$\hat{E}(t) = -if(t)\sum_{q=1}^{q_c}\mathrm{g}(\omega_q)\left(\hat{a}_q^\dagger e^{i\omega_q t} - \hat{a}_q e^{-i\omega_q t}\right), \quad (7.64)$$

$$\hat{A}(t) = -\int \mathrm{d}t\hat{E}(t) = i\sum_{q=1}^{q_c}\mathrm{g}(\omega_q)\left[F_q(t)\hat{a}_q^\dagger - F_q^*(t)\hat{a}_q\right], \quad (7.65)$$

wherein Eq. (7.65) we have defined $F(t) \equiv \int \mathrm{d}t f_q(t)$ with $f_q(t) \equiv f(t)e^{i\omega_q t}$, we can rewrite Eq. (7.63) as

$$i\hbar\frac{\partial}{\partial t}\left|\Phi_{\mathrm{i,hom}}(\mathbf{K},t)\right\rangle = i\sum_{q=1}^{q_c} g(\omega_q)\Bigg[\Big(-M_{\mathrm{i,i}}^{(\mathrm{ter})}(\mathbf{K},t)f_q(t) + M_{\mathrm{i,i}}^{(\mathrm{tra})}(\mathbf{K},t)F_q(t)\Big)\hat{a}_q^\dagger - \Big(-M_{\mathrm{i,i}}^{(\mathrm{ter})}(\mathbf{K},t)f_q^*(t) + M_{\mathrm{i,i}}^{(\mathrm{tra})}(\mathbf{K},t)F_q^*(t)\Big)\hat{a}_q\Bigg]\left|\Phi_{\mathrm{i,hom}}(\mathbf{K},t)\right\rangle. \quad (7.66)$$

As observed, the homogeneous part of this equation is given by a linear combination of creation and annihilation operators acting on the harmonic modes. This equation bears a resemblance to those derived in the analysis of HHG processes in atomic [11–13, 15] and molecular [21] systems. From these analysis, we learned that their solution can be expressed as

$$\left|\Phi_{\mathrm{i,hom}}(\mathbf{K},t)\right\rangle = \hat{\mathcal{D}}\big(\boldsymbol{\chi}_{\mathrm{i}}(\mathbf{K},t,t_0)\big)\left|\Phi_{\mathrm{i,hom}}(\mathbf{K},t_0)\right\rangle, \quad (7.67)$$

where in this expression we have defined

$$\hat{\mathcal{D}}(\boldsymbol{\chi}_{\mathrm{i}}(\mathbf{K},t,t_0)) \equiv \prod_{q=1}^{q_c}[e^{i\varphi_q(\mathbf{K},t,t_0)}\hat{D}_q(\chi_{\mathrm{i}}^{(q)}(\mathbf{K},t,t_0))], \quad (7.68)$$

with $\varphi_q(\mathbf{K}, t, t_0)$ a phase factor arising from the use of the Baker–Campbell–Hausdorff formula [12,13,56] in order to write the solution above, and where $\chi_{\mathrm{i}}^{(q)}(\mathbf{K}, t, t_0)$ is given by

$$\chi_{\mathrm{i}}^{(q)}\big(\mathbf{K}, t, t_0\big) = \frac{1}{\hbar} g(\omega_q) \int_{t_0}^{t} \mathrm{d}\tau \Big[- M_{\mathrm{i,i}}^{(\mathrm{ter})}(\mathbf{K}, \tau) f_q(\tau) + M_{\mathrm{i,i}}^{(\mathrm{tra})}(\mathbf{K}, \tau) F_q(\tau) \Big]. \tag{7.69}$$

Thus, by adding to this solution a particular solution to the inhomogeneous equations, we find the following recursive relation for the solutions of Eqs. (7.62) and (7.61),

$$\begin{aligned} |\Phi_v(\mathbf{K}, t)\rangle &= \hat{\mathcal{D}}\big(\boldsymbol{\chi}_v(\mathbf{K}, t, t_0)\big)\, |\Phi_v(\mathbf{K}, t_0)\rangle \\ &\quad - \frac{i}{\hbar} \int_{t_0}^{t} \mathrm{d}t' \hat{\mathcal{D}}\big(\boldsymbol{\chi}_v(\mathbf{K}, t, t')\big) \hat{\mathcal{M}}_{v,c}(\mathbf{K}, t')\, |\Phi_c(\mathbf{K}, t')\rangle, \end{aligned} \tag{7.70}$$

$$\begin{aligned} |\Phi_c(\mathbf{K}, t)\rangle &= \hat{\mathcal{D}}\big(\boldsymbol{\chi}_c(\mathbf{K}, t, t_0)\big)\, |\Phi_c(\mathbf{K}, t_0)\rangle \\ &\quad - \frac{i}{\hbar} \int_{t_0}^{t} \mathrm{d}t' \hat{\mathcal{D}}\big(\boldsymbol{\chi}_c(\mathbf{K}, t, t')\big) \hat{\mathcal{M}}_{c,v}(\mathbf{K}, t')\, |\Phi_v(\mathbf{K}, t')\rangle, \end{aligned} \tag{7.71}$$

where in this expression we have defined for the sake of clarity

$$\hat{\mathcal{M}}_{\mathrm{i,j}}(\mathbf{K}, t') \equiv M_{\mathrm{i,j}}^{(\mathrm{ter})}(\mathbf{K}, t) \hat{E}(t) + M_{\mathrm{i,j}}^{(\mathrm{tra})} \hat{A}(t). \tag{7.72}$$

By combining these equations, while keeping terms up to first order in $\mathrm{g}(\omega_q)$, we get after introducing the initial conditions

$$|\Phi_v(\mathbf{K}, t)\rangle = \delta(\mathbf{K} - \mathbf{K}_0) \hat{\mathcal{D}}\big(\boldsymbol{\chi}_v(\mathbf{K}, t, t_0)\big) \bigotimes_{q=1}^{q_c} |0_q\rangle \tag{7.73}$$

$$|\Phi_c(\mathbf{K}, t)\rangle = -\delta(\mathbf{K} - \mathbf{K}_0) \frac{i}{\hbar} \int_{t_0}^{t} \mathrm{d}t' \hat{\mathcal{D}}\big(\boldsymbol{\chi}_c(\mathbf{K}, t, t')\big) \hat{\mathcal{M}}_{c,v}(\mathbf{K}, t') \bigotimes_{q=1}^{q_c} |0_q\rangle. \tag{7.74}$$

Likewise, for the joint state of the system we obtain, up to a normalization factor,

$$\begin{aligned} |\tilde{\Psi}'(t)\rangle &= \sum_{m=v,c} \int \mathrm{d}\mathbf{K}\, |\mathbf{K}, m\rangle \otimes |\Phi_m(\mathbf{K}, t)\rangle \\ &= \hat{\mathcal{D}}\big(\boldsymbol{\chi}_v(\mathbf{K}_0, t, t_0)\big)\, |\mathbf{K}_0, v\rangle \bigotimes_{q=1}^{q_c} |0_q\rangle \\ &\quad - \frac{i}{\hbar} \int_{t_0}^{t} \mathrm{d}t' \hat{\mathcal{D}}\big(\boldsymbol{\chi}_c(\mathbf{K}_0, t, t')\big) \hat{\mathcal{M}}_{c,v}(\mathbf{K}_0, t')\, |\mathbf{K}_0, c\rangle \bigotimes_{q=1}^{q_c} |0_q\rangle. \end{aligned} \tag{7.75}$$

It is worth noting that, similar to the quantum optical description of strong-field processes in atomic systems [11–13, 15], for solid-state systems each electromagnetic field mode experiences a displacement by an amount $\chi_{\mathrm{i}}^{(q)}(\mathbf{K}, t, t_0)$. However, given that the electron dynamics in solids are different to those occurring in atomic systems, this quantity gets influenced both by interband and intraband dynamics. In the remainder of this subsection, we study how these two impact the final quantum optical state. Nevertheless, before doing so, we return to the original frame of reference with respect to the electron dynamics, i.e.,

$$|\tilde{\Psi}(t)\rangle = e^{i\mathbf{e}(A_{\mathrm{cl}}(t)+\hat{A}(t))\hat{r}_{i,\mathrm{tra}}/\hbar}\hat{U}_{\mathrm{sc}}(t, t_0)|\tilde{\Psi}'(t_0)\rangle, \tag{7.76}$$

which in the asymptotic limit $t \to \infty$ leads to

$$|\tilde{\Psi}(t)\rangle = \hat{U}_{\mathrm{sc}}(t, t_0)|\tilde{\Psi}'(t_0)\rangle. \tag{7.77}$$

At this point, it is crucial to note that in Eq. (7.76), the unitary transformation $e^{i\mathbf{e}\hat{A}(t)\hat{r}_{i,\mathrm{tra}}/\hbar}$ inherently introduces entanglement between the canonical crystal momentum and the field modes. This arises as $\hat{r}_{i,\mathrm{tra}}$ is not diagonal with respect to $\mathbf{K}$. However, in the discrete mode description employed here, where we introduce the envelope function $f(t)$ to capture the field's envelope, it happens that $\lim_{t\to\infty} f(t) = 0$, leading to $\lim_{t\to\infty} \hat{A}(t) = 0$. Therefore, within the scope of our current framework, this additional operator does not entangle the field and the electron at the final time. Nevertheless, it does introduce entanglement at the intermediate steps of the dynamics, which are essentially caused by the coupling of the intraband dynamics to the different field modes.

The analysis we aim to perform mainly focuses on HHG processes, where the electron ends up in the valence band of the solid-state system. Here, we impose the electron to be found in the valence band by applying the projector operator $\hat{P}_v \equiv \int \mathrm{d}\mathbf{K}\, |\mathbf{K}, v\rangle\langle\mathbf{K}, v|$, and trace out the electronic degrees of freedom. By doing this, while assuming that the probability of finding in the valence band electrons initially born in the conduction band is small, we arrive at

$$|\Phi_v(\mathbf{K}, t)\rangle \approx \hat{\mathcal{D}}\big(\boldsymbol{\chi}_v(\mathbf{K}_0, t, t_0)\big) \bigotimes_{q=1}^{q_c} |0_q\rangle, \tag{7.78}$$

similar to what is found for atomic systems. However, it is important to note here that, in this analysis, we have neglected contributions in the form $\langle\mathbf{K}, v|\, \hat{U}_{\mathrm{sc}}(t, t_0)\, |\mathbf{K}', c\rangle$, which are considerably smaller than the diagonal ones with respect to the valence band as they scale with $\mathrm{g}(\omega_q)$. The

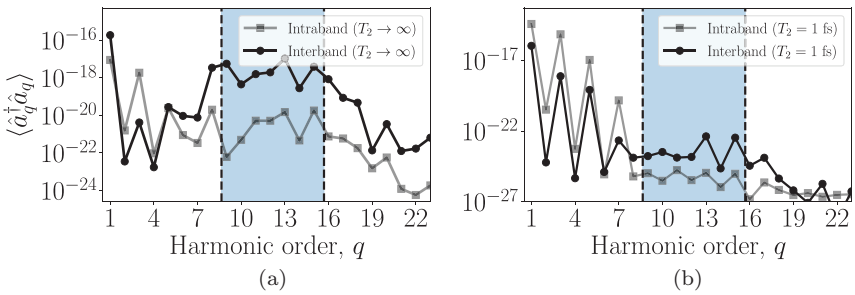

Fig. 7.5 Mean photon numbers calculated for various harmonics using Eq. (7.78). The analysis pertains to the ZnO material under the influence of a linearly polarized laser pulse aligned along the $\Gamma - A$ crystal direction. The laser settings include a peak field strength of 0.5 V/Å, a central wavelength of $\lambda_L = 3.25\,\mu$m, and a duration of $\Delta t \approx 96$ fs (≈9 optical cycles). In panel (a), an ideal solid scenario is depicted, where dephasing effects are absent ($T_2 \to \infty$). In contrast, panel (b) accounts for scenarios where dephasing effects are included. The dashed blue region denotes the minimum and maximum energy band gaps in the specified solid direction.

introduction of these terms would indeed establish entanglement between the electron and electromagnetic field states. However, our subsequent exploration using a Wannier-based analysis — a more convenient representation for light-matter entanglement analyses — reveals that even in the scenario considered here, where ZnO is analyzed, the amount of light-matter entanglement remains marginal even in the many-electron limit.

To validate the outcomes derived from Eq. (7.78), we proceed to evaluate the mean photon number of the various harmonic modes at time $t \to \infty$. To some extent, this observable should mirror the harmonic spectra observed following HHG processes [77]. Figure 7.5 illustrates the outcomes of this computation for both (a) the no-dephasing scenario ($T_2 \to \infty$) and (b) $T_2 = 1$ fs. Notably, the obtained quantity mimics key aspects of the HHG spectra, displaying a plateau region extending from the lowest to the maximum energy band gap, followed by a sharp cutoff. In both cases, the interband component prevails over the intraband one in the non-perturbative (plateau) region. Decreased dephasing values result in better resolved peaks and reduced overall harmonic intensities.

7.3.2.1 *An Extension to the Many-Electron Regime*

It is worth noting that our analysis revolves around the single-electron level. Nonetheless, in a semiconductor's ground state, the valence band

is typically fully occupied, forming what is known as a Fermi sea. Utilizing the semiconductor Bloch equations holds a significant advantage in this scenario, as it inherently incorporates the typically weak many-electron interactions through effective couplings, such as, for instance, dephasing. Therefore, within this framework, each electron can be treated independently, possessing a distinct initial crystal momentum $\mathbf{K}$ spanning the entire Brillouin zone. Consequently, extending Eq. (7.78) to a many-body formulation, we have

$$|\Phi_v(t)\rangle \approx \hat{\mathcal{D}}\left(N_z \int \mathrm{d}\mathbf{K}\boldsymbol{\chi}_v(\mathbf{K},t,t_0)\right)\bigotimes_{q=1}^{q_c}|0_q\rangle,$$

$$= \hat{\mathcal{D}}\big(\bar{\boldsymbol{\chi}}_v(t,t_0)\big)\bigotimes_{q=1}^{q_c}|0_q\rangle, \tag{7.79}$$

where N_z denotes the number of Brillouin zones excited by the laser field. In our numerical analysis, we employed N_z within the range $10^6 - 10^7$, a value subject to variation based on distinct experimental conditions. These conditions involve parameters like the laser beam width, alignment of the crystal lattice concerning the field's polarization, and, in cases where the HHG process occurs during transmission, the sample's width. Such variations can significantly impact the specific value of N_z.

7.3.2.2 *Conditioning on HHG and Its Consequences*

The state presented in Eq. (7.79) corresponds to a classical state. For instance, if one computes the Wigner function of this state — regardless of the chosen harmonic mode — would yield a Gaussian distribution. However, additional operations can be applied to this state to generate non-classical states. In experimental setups [11, 78] extended to solid-state systems [79], the creation of non-classical states of light involves correlation measurements between the different harmonic modes and part of the input fundamental mode. Mathematically, this operation focuses on events where at least one photon is generated in some harmonic mode $q \neq 1$, while considering the correlations that emerge with the fundamental mode. This can be formulated as the projective operation [18, 19]

$$\hat{P}_{\mathrm{cond}} = \mathbb{1} - \bigotimes_{q=1}^{q_c}|0_q\rangle\langle 0_q|, \tag{7.80}$$

which we shall refer to hereafter as the *conditioning on HHG* operation. Applying this operator to the state in Eq. (7.79) leads, up to a normalization

factor, to

$$\left|\bar{\Phi}_v(t)\right\rangle = \bigotimes_{q=1}^{q_c} |\bar{\chi}_v^{(q)}(t,t_0)\rangle - \xi_{\rm IR}\xi_{\rm UV} \bigotimes_{q=1}^{q_c} |0_q\rangle, \tag{7.81}$$

where $\xi_{\rm IR} \equiv \langle 0_q|\bar{\chi}_v^{(q=1)}(t,t_0)\rangle$ and $\xi_{\rm UV} \equiv \prod_{q=2}^{q_c}\langle 0_q|\bar{\chi}_v^{(q)}(t,t_0)\rangle$. This state corresponds to a massively entangled state, where all the harmonic modes that get excited during the HHG process become entangled [19]. However, thus far, the existing experimental implementations focus only on the infrared mode by measuring the intensity of the generated harmonics [11–13,78]. In mathematical terms, this operation corresponds to projecting the conditioned state in Eq. (7.81) with respect to $\bigotimes_{q=2}^{q_c}|\bar{\chi}_v^{(q)}(t,t_0)\rangle$. This actually leads to

$$\left|\bar{\Phi}_{v,\rm IR}(t)\right\rangle = |\bar{\chi}_v^{(q=1)}(t,t_0)\rangle - \xi_{\rm IR}|\xi_{\rm UV}|^2\,|0_{q=1}\rangle, \tag{7.82}$$

which is a superposition between two different coherent states.

In Fig. 7.6, we compute the Wigner function of the state in Eq. (7.82) for the case where ZnO is excited with a linearly polarized laser field along

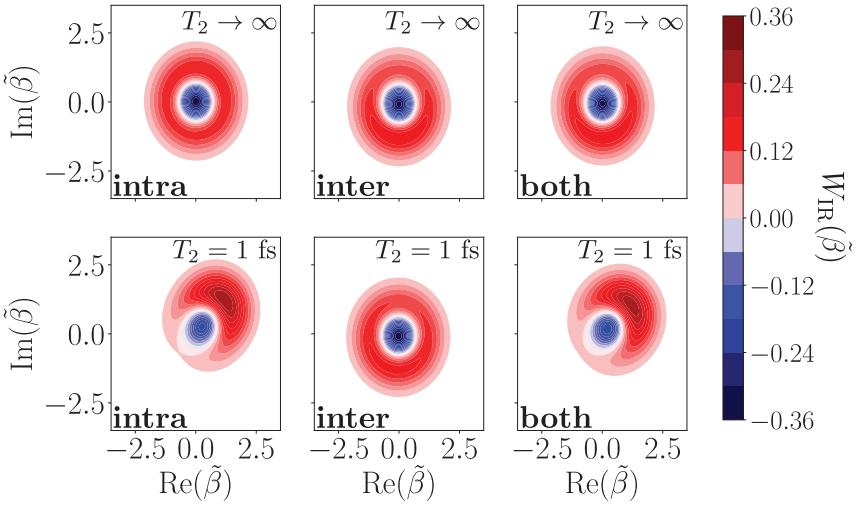

Fig. 7.6 Wigner functions of the state in Eq. (7.82) under various conditions. Each row represents different dephasing times, with the first two columns highlighting the separate contributions of intraband and interband effects (by intentionally disabling the other). The last column displays the combined contribution of both effects. The material analyzed is ZnO, excited with a linearly polarized laser field along the $\Gamma - A$ direction, exciting a total of $N_z = 1.6 \times 10^7$ Brillouin zones. The applied laser field has $\lambda_L = 3.25\,\mu$m, a field strength of $0.5\,$V/Å, and a duration of $\Delta t \approx 96\,$fs (9 optical cycles). Adapted with permission from [32].

the $\Gamma - A$ direction which excites a total of $N_z = 1.6 \times 10^7$ Brillouin zones. We consider the applied laser field to have $\lambda_L = 3.25\,\mu$m, a field strength of $0.5\,\mathrm{V/Å}$ and a duration of $\Delta t \approx 96\,$fs, corresponding to 9 optical cycles. In the first row, we show an ideal scenario without the introduction of dephasing, while in the second row a dephasing time $T_2 = 1\,$fs has been set. On the other hand, each column corresponds to different contributions: intraband, interband and the combination of both, from left to right respectively. As observed, these results show that: (1) reduced values of T_2 lead to more unbalanced coherent state superpositions, yielding less homogeneous Wigner functions; and (2) that intraband effects seem to be dominant in dictating the shape of the final Wigner function. This can be understood by considering that a smaller dephasing time leads the electron to spend more time in the valence band, consequently increasing the contribution from intraband effects compared to interband effects.

Contrasting behaviors with respect to those found for the Wigner function are observed for the amount of entanglement between the infrared mode and the other harmonics, as shown in Fig. 7.7. The degree of entanglement in these scenarios is contingent upon the radiation generated in the harmonic modes, where the perturbative (plateau) region is primarily influenced by interband effects, as depicted in panel (a). In this case, interband effects dominate over intraband ones. Conversely, as shown in panel (b), the presence of dephasing effects significantly impacts the overall entanglement. Specifically, when considering $T_2 = 1\,$fs, instead of no

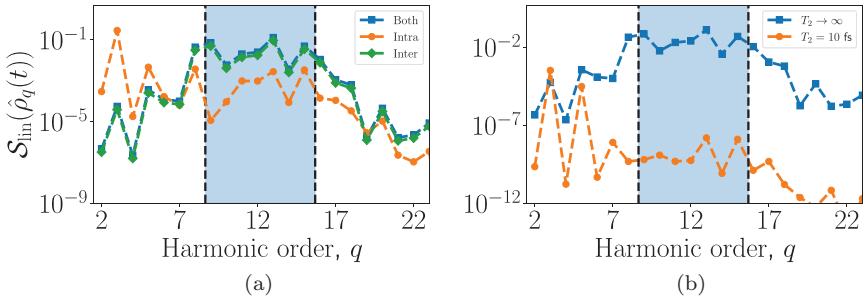

Fig. 7.7 The degree of entanglement between the fundamental mode and the qth harmonic mode is plotted against the harmonic order. Panel (a) demonstrates the distinct impacts of interband and intraband effects individually, along with their combined effect. Panel (b) showcases the effect of dephasing on this measure of entanglement. Identical excitation conditions to those in Fig. 7.6 have been applied.

dephasing effects, we observe a reduction of approximately nine orders of magnitude in these entanglement values.

7.3.3 *Wannier-Bloch Picture*

The use of a discrete basis set, such as the Wannier states, in the quantum optical analysis of HHG processes in solids provides a more manageable framework for exploring the entanglement between light and matter. Consequently, in this section, we aim to address the solution to the Schrödinger equation presented in Eq. (7.9) by employing a hybrid Wannier-Bloch basis representation akin to the methodology outlined in Section 7.2.2. To achieve this, we formulate the Schrödinger equation as

$$i\hbar\frac{\partial\,|\Psi(t)\rangle}{\partial t} = \big[\hat{H}_{\rm cr} + \mathsf{e}\hat{r}\hat{E}(t) + \hat{H}_{\rm field}\big], \tag{7.83}$$

where, unlike Eq. (7.9), here we do not explicitly differentiate between the intraband and interband components of the position operator. For the sake of simplicity, adhering to a single-active electron description similar to that of Section 7.2.2, we represent their initial state as

$$|\Psi(t_0)\rangle = |w_{j_0,v}\rangle \otimes |\alpha_L\rangle \bigotimes_{q=2}^{q_c} |0_q\rangle, \tag{7.84}$$

where the single-active electron initially occupies the j_0th Wannier site.

By applying similar unitary transformations as conducted in Section 7.3.2, excluding $e^{i\mathsf{e}(\hat{A}_{\rm cl}(t)+\hat{A}(t))\hat{r}_{i,\rm tra}/\hbar}$, we can rewrite Eq. (7.83) as follows

$$i\hbar\frac{\partial|\tilde{\Psi}'(t)\rangle}{\partial t} = \mathsf{e}\hat{r}(t)\hat{E}(t)|\tilde{\Psi}'(t)\rangle, \tag{7.85}$$

where $\hat{r}(t) \equiv \hat{U}^{\dagger}_{\rm sc}(t)\hat{\hat{r}}\hat{U}_{\rm sc}(t)$. This is the pivotal point where the main distinction between the two approaches becomes evident. Here, the identity in the Wannier-Bloch approximation is introduced, namely

$$\mathbb{1} = \sum_j |w_{j,v}\rangle\langle w_{j,v}| + \int \mathrm{d}\mathbf{k}\,|\phi_{\mathbf{k},c}\rangle\langle\phi_{\mathbf{k},c}|, \tag{7.86}$$

which inputted in Eq. (7.85) leads to

$$\begin{aligned} i\hbar\frac{\partial|\tilde{\Psi}'(t)\rangle}{\partial t} = \mathsf{e}\sum_j \hat{r}(t)\hat{E}(t)\,\langle w_{j,v}|\tilde{\Psi}'(t)\rangle\,|w_{j,v}\rangle \\ + \mathsf{e}\int \mathrm{d}\mathbf{k}\;\hat{r}(t)\hat{E}(t)\,\langle\phi_{\mathbf{k},c}|\tilde{\Psi}'(t)\rangle\,|\phi_{\mathbf{k},c}\rangle. \end{aligned} \tag{7.87}$$

In the following, we perform a similar assumption to that at the conclusion of the Bloch basis analysis in Section 7.3.2. This assumption involves considering the probability of residing in the conduction band to be extremely minimal at all times. We anticipate this approximation to be valid within the realm of weak depletion of the valence band, a scenario aligning with the frequencies and field strengths employed here [38]. Consequently, we approximate Eq. (7.54) as

$$i\hbar\frac{\partial|\tilde{\Psi}'(t)\rangle}{\partial t} \approx \mathsf{e}\sum_j \hat{r}(t)\hat{E}(t)\,\langle w_{j,v}|\tilde{\Psi}'(t)\rangle\,|w_{j,v}\rangle, \tag{7.88}$$

and by projecting with respect to the set of Wannier states, we arrive at the following system of differential equations

$$i\hbar\frac{\partial\,|\Phi_i(t)\rangle}{\partial t} = \sum_j M_{i,j}(t)\hat{E}(t)\,|\Phi_j(t)\rangle, \quad \forall j \in \mathbb{W}, \tag{7.89}$$

where we have defined $|\Phi_i(t)\rangle \equiv \langle w_{i,v}|\tilde{\Psi}(t)\rangle$ and $M_{i,j}(t) \equiv \mathsf{e}\,\langle w_{i,v}|\,\hat{r}(t)\,|w_{j,v}\rangle$. It is worth noting that $M_{i,j}(t)$ is a non-diagonal matrix since an electron initially on site i can end up in site j either through an intra-band transition, described by off-diagonal elements, or via an excitation-recombination mechanism, mainly described by the diagonal elements.

In the following, we investigate HHG processes under the regime of weak electron delocalization, that is, $|M_{i,j}(t)| \ll |M_{i,i}(t)|$ with $i \neq j$. For simplicity, we solely consider nearest neighbor contributions, restricting our focus to the non-diagonal elements of $M_{i,j}(t)$ for which $j = i \pm 1$. Treating these as a perturbation parameter, we expand our state $|\Phi_i(t)\rangle$ up to first order as

$$|\Phi_i(t)\rangle \approx |\Phi_i^{(0)}(t)\rangle + |\Phi_i^{(1)}(t)\rangle, \tag{7.90}$$

such that the zeroth-order term satisfies

$$i\hbar\frac{\mathrm{d}|\Phi_i^{(0)}(t)\rangle}{\mathrm{d}t} = M_{i,i}(t)\hat{E}(t)|\Phi_i^{(0)}(t)\rangle, \tag{7.91}$$

and whose solution can be written as

$$\begin{aligned}|\Phi_i^{(0)}(t)\rangle &= \hat{\mathcal{D}}\big(\boldsymbol{\chi}_{i,i}(t,t_0)\big)|\Phi_i^{(0)}(t_0)\rangle \\ &\equiv \prod_q e^{i\varphi_{i,i}^{(q)}(t,t_0)}\hat{D}_q\big(\chi_{i,i}^{(q)}(t,t_0)\big)|\Phi_i^{(0)}(t_0)\rangle,\end{aligned} \tag{7.92}$$

where $\hat{D}_q(\alpha) = \exp\left[\alpha\hat{a}_q^\dagger - \alpha^*\hat{a}_q\right]$ is the displacement operator acting on mode q, $\varphi_{i,i}^{(q)}(t)$ is a prefactor arising from applying the Baker–Campbell–Hausdorff relation, and $\chi_{i,i}^{(q)}(t,t_0)$ is a coherent state amplitude given by

$$\chi_{i,i}^{(q)}(t,t_0) = -\frac{1}{\hbar}\int_{t_0}^{t} \mathrm{d}\tau e^{i\omega_q\tau}\mathrm{g}(\omega_q)M_{i,i}(\tau). \tag{7.93}$$

It is important to note that, while we have explicitly depicted the dependence of $\chi_{i,i}^{(q)}(t,t_0)$ on the Wannier site, specifically the ith site, the dynamics across all sites are equivalent. Consequently, they result in identical HHG spectra, enabling us to disregard the i index in $\chi_{i,i}^{(q)}(t,t_0)$. Nevertheless, for the sake of completeness, we maintain this notation in the subsequent discussion.

Regarding the first-order term we get the following differential equation

$$\begin{aligned} i\hbar\frac{\mathrm{d}|\Phi_i^{(1)}(t)\rangle}{\mathrm{d}t} &= M_{i,i}(t)\cdot\hat{E}(t)|\Phi_i^{(1)}(t)\rangle \\ &\quad + \sum_{j\in\{i\pm1\}} M_{i,j}(t)\hat{E}(t)|\Phi_j^{(0)}(t)\rangle, \end{aligned} \tag{7.94}$$

whose solution can be generally written as

$$\begin{aligned} |\Phi_i^{(1)}(t)\rangle &= \hat{\mathcal{D}}\big(\boldsymbol{\chi}_{i,i}(t,t_0)\big)|\Phi_i^{(1)}(t_0)\rangle \\ &\quad - \frac{i}{\hbar}\sum_{j\in\{i\pm1\}}\int_{t_0}^{t}\mathrm{d}t'\hat{\mathcal{D}}\big(\boldsymbol{\chi}_{i,i}(t,t')\big)M_{i,j}(t')\hat{E}(t') \\ &\quad \times\hat{\mathcal{D}}\big(\boldsymbol{\chi}_{j,j}(t',t_0)\big)|\Phi_j^{(0)}(t_0)\rangle. \end{aligned} \tag{7.95}$$

Introducing the initial conditions at this point, we observe two distinct contributions based on the final site, j, where the electron ends up:

- If the electron concludes its dynamics in the initial Wannier site, j_0, then the final state is given by

$$|\Phi_{j_0}(t)\rangle = \hat{\mathcal{D}}\big(\boldsymbol{\chi}_{i,i}(t,t_0)\big)\bigotimes_q|0_q\rangle; \tag{7.96}$$

- Conversely, if the electron concludes its dynamics in a different Wannier site from where it started, j, the final state becomes

$$\begin{aligned} |\Phi_j(t)\rangle &= -\frac{i}{\hbar}\int_{t_0}^{t}\mathrm{d}t'\hat{\mathcal{D}}\big(\boldsymbol{\chi}_{j,j}(t,t')\big)M_{j,j_0}(t')\cdot\hat{E}(t') \\ &\quad \times\hat{\mathcal{D}}\big(\boldsymbol{\chi}_{j_0,j_0}(t',t_0)\big)\bigotimes_q|0_q\rangle. \end{aligned} \tag{7.97}$$

It is worth noting that, by taking into account that $\chi^{(q)}_{i,i}(t) = \chi^{(q)}_{j,j}(t) = \chi_q(t)$, we can rewrite Eq. (7.97) as

$$\begin{aligned}|\Phi_j(t)\rangle = -\frac{i}{\hbar}e^{i\varphi(t)}\hat{\mathcal{D}}\big(\boldsymbol{\chi}(t,t_0)\big) \\ \times \int_{t_0}^{t} \mathrm{d}t' e^{-i\theta(t')}\hat{\mathcal{D}}^{\dagger}\big(\boldsymbol{\chi}(t',t_0)\big) \\ \times \big(M_{j,j_0}(t')\hat{E}(t')\big)\hat{\mathcal{D}}\big(\boldsymbol{\chi}(t',t_0)\big)\bigotimes_{q=1}|0_q\rangle,\end{aligned} \tag{7.98}$$

where we have defined $\theta(t') \equiv \sum_q \mathrm{Im}\big\{\chi_q(t,t_0)\chi_q^*(t',t_0)\big\}$. Furthermore, from numerical analysis, we find that the integral above differ in the fifth significant decimal when $j = \pm 1$. Hence, in the following we approximate $|\Phi_{+1}(t)\rangle \approx |\Phi_{-1}(t)\rangle \equiv |\Phi_{\mathrm{NN}}(t)\rangle$.

For a one-dimensional lattice, the joint state of the system can be written as

$$|\tilde{\Psi}'(t)\rangle = |w_{j_0,v}\rangle \otimes |\Phi_{j_0}(t)\rangle + \sqrt{2}\,|w_{\mathrm{NN},v}\rangle \otimes |\Phi_{\mathrm{NN}}(t)\rangle, \tag{7.99}$$

where we defined $|w_{\mathrm{NN},v}\rangle = (1/\sqrt{2})(|w_{j_0+1,v}\rangle + |w_{j_0-1,v}\rangle)$. If we denote the coordinate number of the lattice by f_{c} (i.e., $f_{\mathrm{c}} = 2d$ in hypercubic lattices in d-dimensions, $f_{\mathrm{c}} = 3$ for honeycomb lattice in 2D, $f_{\mathrm{c}} = 6$ for triangular lattice in 2D), we can provide a generalization of our state to arbitrary dimensions

$$|\tilde{\Psi}'(t)\rangle = |w_{j_0,v}\rangle \otimes |\Phi_{j_0}(t)\rangle + \sqrt{f_{\mathrm{c}}}\,|w_{\mathrm{NN},v}\rangle \otimes |\Phi_{\mathrm{NN}}(t)\rangle, \tag{7.100}$$

where now $|w_{\mathrm{NN},v}\rangle = (1/\sqrt{f_{\mathrm{c}}})(\sum_{j\in\mathrm{NN}}|w_{j_0+j,v}\rangle)$.

7.3.3.1 *An Extension to the Many-Electron Regime*

Although until now we have worked under the single-active electron approximation, as mentioned in the Bloch-Bloch analysis of Sec. 7.3.2, the initial state of the system corresponds to a completely filled Fermi sea, i.e., all Wannier sites are occupied. Given that electron-electron correlations are weak in typical semiconductor materials, we can consequently treat the interaction of all electrons with the laser field as independent. Thus, by introducing the same unitary transformations as for the single-electron analysis, and neglecting the contributions of the conduction band, the Schrödinger equation reads

$$i\hbar\frac{\mathrm{d}|\tilde{\Psi}'(t)\rangle}{\mathrm{d}t} \approx \mathsf{e}\sum_{\mathbf{m}}\hat{\tilde{r}}(t)\hat{E}(t)\langle w_{\mathbf{m},v}|\tilde{\Psi}'(t)\rangle\,|w_{\mathbf{m},v}\rangle, \tag{7.101}$$

where $|w_{\mathbf{m},v}\rangle \equiv |w_{m_0,v}\rangle \otimes |w_{m_1,v}\rangle \otimes \cdots \otimes |w_{m_{N_\mathsf{e}},v}\rangle$; and $\hat{\tilde{R}} = \sum_{j=0}^{N_\mathsf{e}-1} \hat{r}_{i,j}$, with N_e being the number of electrons contributing in a phase-matched way to the HHG process, and $r_{i,j}$ the position operator along direction i acting on the jth electron.

Similarly to before, we assume the regime of weak delocalization, ensuring the single-electron wavepacket does not significantly spread across different Wannier sites. Consequently, we separate the contribution of $\tilde{r}(t)$ into diagonal and off-diagonal elements, allowing us to treat the latter using perturbation theory. Thus, by projecting Eq. (7.101) with respect to $|w_{\mathbf{i},v}\rangle$, we obtain

$$i\hbar \frac{\mathrm{d}\,|\Phi_\mathbf{i}(t)\rangle}{\mathrm{d}t} = \mathsf{e} \sum_\mathbf{m} \langle w_{\mathbf{i},v}|\tilde{r}(t)|w_{\mathbf{m},v}\rangle\, \hat{E}(t)\,|\Phi_\mathbf{m}(t)\rangle, \tag{7.102}$$

where we have defined $|\Phi_\mathbf{i}(t)\rangle = \big\langle w_{\mathbf{i},v}|\tilde{\psi}(t)\big\rangle$, and where the matrix elements of $\tilde{r}(t)$ are given by

$$\langle w_{\mathbf{n},v}|\tilde{r}(t)|w_{\mathbf{m},v}\rangle = \sum_{j=0}^{N_\mathsf{e}-1} \big\langle w_{n_j,v}\big|\hat{r}_{i,j}\big|w_{m_j,v}\big\rangle \prod_{l\in\mathcal{O}_j} \delta_{n_l,m_l}, \tag{7.103}$$

wherein the previous expression $\mathcal{O}_j := \{l : l \in \mathbb{N} - \{j\}\}$.

Up to the first order in perturbation theory, the equations we get are identical to the ones found in the single-electron regime. Thus, taking into account the initial conditions, we find two kinds of contributions depending on the final sites j where the electrons end up in:

- If the electrons end up in the initial Wannier sites where they were initially located, then the final state reads

$$|\Phi_\mathbf{i}(t)\rangle = \hat{\mathcal{D}}\big(N_\mathsf{e}\boldsymbol{\chi}(t,t_0)\big) \bigotimes_q |0_q\rangle; \tag{7.104}$$

- If one of the electrons ends up in a different Wannier site j from which it initially started the dynamics, then the final state reads

$$\begin{aligned} |\Phi_\mathbf{i}(t)\rangle = -\frac{i}{\hbar}&\hat{\mathcal{D}}\big(N_\mathsf{e}\boldsymbol{\chi}(t,t_0)\big) \\ &\times \int_{t_0}^{t} \mathrm{d}t' e^{-i\theta(t,t',t_0)} M_{i_n,i_{n,0}}(t') \\ &\times \hat{\mathcal{D}}^\dagger\big(N_\mathsf{e}\boldsymbol{\chi}(t',t_0)\big)\hat{E}(t')\hat{\mathcal{D}}\big(N_\mathsf{e}\boldsymbol{\chi}(t',t_0)\big) \\ &\bigotimes_q |0_q\rangle, \end{aligned} \tag{7.105}$$

where we have considered that one of the electrons has transitioned from its initial site $i_{n,0}$ to site i_n. It is worth noting that the first-order perturbation theory term describes events where only one of the electrons ends up in a different Wannier site from which it initially started the dynamics. In order to consider events where we find n transitions, we then have to perform a perturbation theory expansion up to the nth order term. However, in the many-electron scenario, we restrict ourselves to solids for which the HHG process is highly localized, as it happens for instance with solid argon [80], or for specific crystal directions of certain solids like ZnO (see Fig. 7.2).

With all this, we can extend Eq. (7.100) to the many-electron scenario as

$$|\tilde{\Psi}'(t)\rangle = |w_{\boldsymbol{j_0},v}\rangle \otimes |\Phi_{\boldsymbol{j_0}}(t)\rangle + \sqrt{f_c N_{\mathsf{e}}}|w_{\overline{\mathrm{NN}},v}\rangle \otimes |\Phi_{\overline{\mathrm{NN}}}(t)\rangle, \tag{7.106}$$

where it is worth noting that, like in Eq. (7.75), we get an entangled state between light and matter. However, the main advantage in this case is that we have characterized the electronic states through a discrete basis set. This allows us to perform a simple light-matter entanglement characterization, assessing whether the approximations performed in the many-body analysis, which essentially neglect the entanglement between light and matter, hold valid for the considered material.

7.3.3.2 *Conditioning on HHG and Its Consequences*

To compare the implications of the light-matter entanglement outlined in Eq. (7.106) against the findings in Section 7.3.2, we consider here the use of the conditioning on HHG operation presented in Eq. (7.80). By applying this operation to Eq. (7.106) and subsequently projecting it onto the coherent state $|\boldsymbol{\gamma}\rangle \equiv \bigotimes_{q\geq 2} |\chi_q(t,t_0)\rangle$, representing the measured harmonics, we obtain

$$|\Psi_{\mathrm{cond}}(t)\rangle = \langle \boldsymbol{\gamma}|\Psi(t)\rangle - \xi(\boldsymbol{\gamma},t)\,|\alpha_L\rangle, \tag{7.107}$$

with $\xi(\boldsymbol{\gamma},t) = \langle \alpha, 0_{\mathrm{HH}}|\Psi(t)\rangle\,\langle \boldsymbol{\gamma}|0_{\mathrm{HH}}\rangle$.

We begin the comparison by first computing the Wigner function of the infrared field mode. However, unlike the Bloch-basis analysis, in this scenario we include in our state the possibility of the electrons ending up in a valence band state different from the initial one. Therefore, assuming a lack of knowledge about the final state with which the electron has recombined, we can express the quantum optical state of the system in terms of the

following density matrix

$$\hat{\rho}_{\text{field}}(t) = \text{tr}_{\text{elec}}(|\Psi_{\text{cond}}(t)\rangle\langle\Psi_{\text{cond}}(t)|), \tag{7.108}$$

where we have essentially traced out the electronic degrees of freedom.

When exploring the interaction between ZnO and a linearly polarized electric field along the $\Gamma - A$ crystal direction, featuring a peak field strength $E_0 \approx 0.2\,\text{V/Å}$, $\lambda_L = 3.25\,\mu\text{m}$ and duration $\Delta t \approx 40\,\text{fs}$, we arrive at the Wigner functions shown in Fig. 7.8. Each panel corresponds to a different number of electrons N_e, specifically $N_\text{e} = 1\times10^7, 1\times10^8, 5\times10^8$ and 1×10^9 from panels (a) to (d), respectively. Notably, these results do not account for dephasing effects, yet exhibit a strong resemblance to those illustrated in Fig. 7.6 (c) from the Bloch-based analysis, where $N_z = 1.6\times10^7$.

Furthermore, as can be seen here, explicitly increasing the number of electrons contributing in a phase-matched way to the HHG process leads to a Wigner distribution that shifts from a displaced Fock state

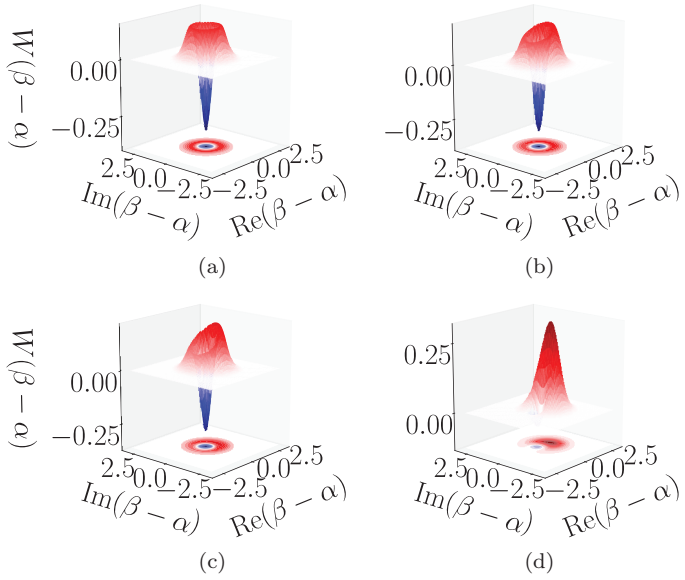

Fig. 7.8 Wigner function of the state in Eq. (7.108) when considering different numbers of electrons independently contributing to the HHG process. Specifically, from (a) to (d), the values $N_\text{e} = 1\times10^7, 1\times10^8, 5\times10^8$ and 1×10^9 have been used. Here, we consider the interaction of ZnO with a linearly polarized electric field along the $\Gamma - A$ crystal direction, with peak field strength $E_0 \approx 0.2\,\text{V/Å}$, $\lambda_L = 3.25\,\mu\text{m}$ and duration $\Delta t \approx 40\,\text{fs}$ (≈4 optical cycles). Adapted with permission from https://arxiv.org/abs/2211.00033.

(Fig. 7.8 (a)), to an unbalanced superposition between two close coherent states (Fig. 7.8 (b) and (c)) until it reaches a regime where one of the coherent states in the superposition dominates (Fig. 7.8 (d)). This behavior bears resemblance to what is found for atomic HHG [11–13, 15], which is a consequence of the natural localization of the HHG process in atomic and molecular targets. However, and as mentioned earlier, in this case the electron dynamics are different to the case of atoms, and they lead to non-trivial consequences on the generated coherent state superpositions.

As was already stated, a main advantage of introducing a Wannier-based analysis lies in the discreteness of the electronic basis set. This discretization significantly simplifies the characterization of entanglement compared to continuous-variable basis sets, as observed for the Bloch-based approach outlined in Section 7.3.2. Moreover, working within the regime of weak delocalization allows us to focus on nearest-neighbor interactions, further streamlining the entanglement analysis. This particular simplification stems from treating the electronic degrees of freedom in Eq. (7.106) as qubits. Consequently, the entanglement entropy in Eq. (7.43) serves as a suitable entanglement measure. Additionally, examining the fidelity of the state with respect to the $|w_{\overline{\mathrm{NN}},v}\rangle$, offers insights into the likelihood of finding electrons in their nearest neighbors. For a generic density matrix $\hat{\sigma}$, this quantity can be computed as follows

$$\mathcal{F}_{\mathrm{del}}(\hat{\sigma}) = \mathrm{tr}_{\mathrm{field}}\left(\langle w_{\overline{\mathrm{NN}},v}|\hat{\sigma}|w_{\overline{\mathrm{NN}},v}\rangle\right). \tag{7.109}$$

In Fig. 7.9, we illustrate these two quantities for different lattice geometries, and their dependency on the number of electrons N_{e}. More specifically, panel (a) demonstrates the fidelity, while panel (b) showcases the entanglement entropy. The dashed curves represent the state without conditioning, i.e., when considering Eq. (7.106). On the other hand, the solid curves depict the case with Eq. (7.107), where the conditioning on HHG operation has been applied. Throughout both cases, the observed values of these measures generally remain within the order of 10^{-6} at maximum. This observation suggests that, under the considered excitation conditions, the entanglement features are nearly negligible. This underscores the validity of the approximations utilized in Section 7.3.2. Nevertheless, there is a noticeable trend: the amount of entanglement tends to increase with the number of electrons involved in the interaction region. However, for larger values of N_{e}, introducing more than nearest neighbors might become necessary.

Despite the notably reduced values observed for the degree of entanglement and the fidelity in Fig. 7.9, several noteworthy features emerge.

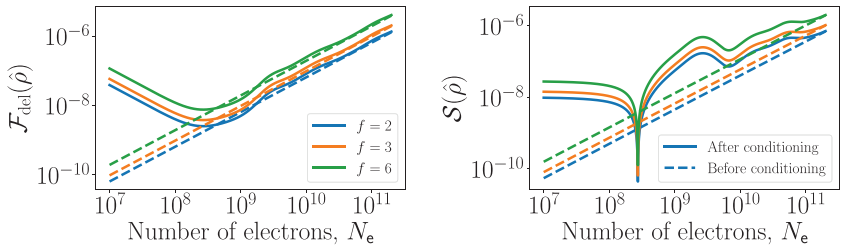

Fig. 7.9 In (a), the fidelity measure outlined in Eq. (7.109) is plotted against the number of electrons contributing independently to the HHG process. In (b), the entanglement entropy is depicted instead. Dashed lines represent scenarios without conditioning on HHG operation, while continuous curves signify cases where this conditioning has been applied. Each color corresponds to a different coordinate number. The laser-solid interaction conditions mirror those of Fig. 7.8. Adapted with permission from https://arxiv.org/abs/2211.00033.

Firstly, for $N_{\rm e} \lesssim 2 \times 10^8$, both the fidelity and the entanglement after the conditioning (solid curves) exhibit higher values compared to those before the conditioning (dashed curves). This enhancement is primarily attributed to $|\boldsymbol{\chi}(t, t_0)|$, which remains a small quantity ($\sim 10^{-2}$), allowing the conditioning to accentuate the contributions from electron recombination in the nearest neighbors. Consequently, this increase in fidelity is accompanied by a growth in the value of $\mathcal{S}(\hat{\rho})$. Secondly, an intriguing observation occurs around $N_{\rm e} \simeq 2.5 \times 10^8$: an abrupt drop in $\mathcal{S}(\hat{\rho})$ after the conditioning, which is absent for $\mathcal{F}_{\rm del}(\hat{\rho})$. This phenomenon stems from the cancellation of quantum optical contributions arising from the $|w_{\overline{\rm NN},v}\rangle$ term in Eq. (7.107), i.e., $\langle \boldsymbol{\gamma} | \Phi_{\overline{\rm NN}}(t) \rangle - \xi(\boldsymbol{\gamma}, t) \, |\alpha_L\rangle$. As $N_{\rm e}$ increases, $\xi(\boldsymbol{\gamma}, t)$ diminishes with the increment of $|\boldsymbol{\chi}(t, t_0)|$, resulting in a minimal overlap with the initial state. Consequently, in this regime where the conditioning on HHG operation exhibits this minimal effect, $\mathcal{F}_{\rm del}(\hat{\rho})$ and $\mathcal{S}(\hat{\rho})$ for the state before and after conditioning coincide. Furthermore, it is important to note that these two quantities demonstrate a marginal increment with the coordinate number f_c, despite the modifications being far from noticeable.

7.4 Outlook

In this chapter, we have provided an in-depth study of strongly driven laser-solid interactions from a quantum optical perspective. This analysis, focused

on solids exhibiting minimal electron-electron correlations, produces outcomes akin to those observed in atomic systems [15] and molecular setups [21]. Rather than disheartening, these aligned findings serve as a catalyst for transitioning from prevailing atomic-based experimental platforms to solid-state counterparts. Notably, considering the diminutive sizes of typical semiconductor samples [34, 47] — integral components in existing technologies — the similarity in observed results following strong laser-solid interactions suggests the feasibility of conducting these experiments on a smaller scale. This marks the initial stride from fundamental physics inquiries toward practical technological advancements.

Acknowledgments

ICFO group acknowledges support from: ERC AdG NOQIA; MICIN/AEI (PGC2018-0910.13039/501100011033, CEX2019-000910-S/10.13039/501100011033, Plan National FIDEUA PID2019-106901GB-I00, FPI; MICIIN with funding from European Union NextGenerationEU (PRTR-C17.I1): QUANTERA MAQS PCI2019-111828-2); MCIN/AEI/10.13039/501100011033 and by the "European Union NextGeneration EU/PRTR" QUANTERA DYNAMITE PCI2022-132919 within the QuantERA II Programme that has received funding from the European Union's Horizon 2020 research and innovation programme under Grant Agreement No 101017733Proyectos de I+D+I "Retos Colaboración" QUSPIN RTC2019-007196-7); Fundació Cellex; Fundació Mir-Puig; Generalitat de Catalunya (European Social Fund FEDER and CERCA program, AGAUR Grant No. 2021 SGR 01452, QuantumCAT U16-011424, co-funded by ERDF Operational Program of Catalonia 2014-2020); Barcelona Supercomputing Center MareNostrum (FI-2023-1-0013); EU (PASQuanS2.1, 101113690); EU Horizon 2020 FET-OPEN OPTOlogic (Grant No 899794); EU Horizon Europe Program (Grant Agreement 101080086 — NeQST), National Science Centre, Poland (Symfonia Grant No. 2016/20/W/ST4/00314); ICFO Internal "QuantumGaudi" project; European Union's Horizon 2020 research and innovation program under the Marie-Skłodowska-Curie grant agreement No 101029393 (STREDCH) and No 847648 ("La Caixa" Junior Leaders fellowships ID100010434: LCF/BQ/PI19/11690013, LCF/BQ/PI20/11760031, LCF/BQ/PR20/11770012, LCF/BQ/PR21/11840013). Views and opinions expressed are, however, those of the author(s) only and do not necessarily reflect those of the European Union, European Commission, European Climate, Infrastructure and Environment Executive Agency (CINEA), nor

any other granting authority. Neither the European Union nor any granting authority can be held responsible for them.

P. Tzallas group at FORTH acknowledges support from: LASERLABEUROPE V (H2020-EU.1.4.1.2 grant no.871124), the H2020 project IMPULSE (GA 871161) and ELI–ALPS. ELI–ALPS is supported by the European Union and co-financed by the European Regional Development Fund (GINOP Grant No. 2.3.6-15-2015-00001).

J. R-D. acknowledges funding from the Government of Spain (Severo Ochoa CEX2019-000910-S and TRANQI), Fundació Cellex, Fundació Mir-Puig, Generalitat de Catalunya (CERCA program) and the ERC AdG CERQUTE.

P. S. acknowledges funding from the European Union's Horizon 2020 research and innovation programme under the Marie Skłodowska-Curie grant agreement No 847517.

A. S. M. acknowledges funding support from the European Union's Horizon 2020 research and innovation programme under the Marie Skłodowska-Curie grant agreement, SSFI No. 887153.

E. P. acknowledges the Royal Society for University Research Fellowship funding under URF\R1\211390.

M. F. C. acknowledges support by the National Key Research and Development Program of China (Grant No. 2023YFA1407100), Guangdong Province Science and Technology Major Project (Future functional materials under extreme conditions - 2021B0301030005) and the Guangdong Natural Science Foundation (General Program project No. 2023A1515010871).

References

[1] A. Gilchrist, K. Nemoto, W. J. Munro, T. C. Ralph, S. Glancy, S. L. Braunstein and G. J. Milburn, Schrödinger cats and their power for quantum information processing, *Journal of Optics B: Quantum and Semiclassical Optics* **6**, 8, p. S828 (2004).

[2] N. Gisin and R. Thew, Quantum communication, *Nature Photonics* **1**, 3, pp. 165–171 (2007).

[3] J. L. O'Brien, A. Furusawa and J. Vučković, Photonic quantum technologies, *Nature Photonics* **3**, 12, pp. 687–695 (2009).

[4] D. V. Strekalov and G. Leuchs, Nonlinear Interactions and Non-classical Light, in R. W. Boyd, S. G. Lukishova and V. N. Zadkov (Eds.), *Quantum Photonics: Pioneering Advances and Emerging Applications*, Springer, pp. 51–101 (2019).

[5] P. G. Kwiat, K. Mattle, H. Weinfurter, A. Zeilinger, A. V. Sergienko and Y. Shih, New high-intensity source of polarization-entangled photon pairs, *Physical Review Letters* **75**, 24, pp. 4337–4341 (1995).

[6] A. McPherson, G. Gibson, H. Jara, U. Johann, T. S. Luk, I. A. McIntyre, K. Boyer and C. K. Rhodes, Studies of multiphoton production of vacuum-ultraviolet radiation in the rare gases, *JOSA B* **4**, 4, pp. 595–601 (1987).

[7] M. Ferray, A. L'Huillier, X. F. Li, L. A. Lompre, G. Mainfray and C. Manus, Multiple-harmonic conversion of 1064 nm radiation in rare gases, *Journal of Physics B: Atomic, Molecular and Optical Physics* **21**, 3, p. L31 (1988).

[8] T. Popmintchev, M.-C. Chen, D. Popmintchev, P. Arpin, S. Brown, S. Ališauskas, G. Andriukaitis, T. Balčiunas, O. D. Mücke, A. Pugzlys, A. Baltuška, B. Shim, S. E. Schrauth, A. Gaeta, C. Hernández-García, L. Plaja, A. Becker, A. Jaron-Becker, M. M. Murnane and H. C. Kapteyn, Bright coherent ultrahigh harmonics in the keV X-ray regime from mid-infrared femtosecond lasers, *Science* **336**, 6086, pp. 1287–1291 (2012).

[9] J. Rivera-Dean, *Quantum-optical analysis of high-order harmonic generation*, Master thesis, Universitat Politècnica de Catalunya (2019), https://upcommons.upc.edu/handle/2117/168580.

[10] A. Gorlach, O. Neufeld, N. Rivera, O. Cohen and I. Kaminer, The quantum-optical nature of high harmonic generation, *Nature Communications* **11**, 1, p. 4598 (2020).

[11] M. Lewenstein, M. F. Ciappina, E. Pisanty, J. Rivera-Dean, P. Stammer, T. Lamprou and P. Tzallas, Generation of optical Schrödinger cat states in intense laser–matter interactions, *Nature Physics* **17**, 10, pp. 1104–1108 (2021).

[12] J. Rivera-Dean, T. Lamprou, E. Pisanty, P. Stammer, A. F. Ordóñez, A. S. Maxwell, M. F. Ciappina, M. Lewenstein and P. Tzallas, Strong laser fields and their power to generate controllable high-photon-number coherent-state superpositions, *Physical Review A* **105**, 3, p. 033714 (2022).

[13] P. Stammer, J. Rivera-Dean, A. Maxwell, T. Lamprou, A. Ordóñez, M. F. Ciappina, P. Tzallas and M. Lewenstein, Quantum electrodynamics of intense laser-matter interactions: A tool for quantum state engineering, *PRX Quantum* **4**, 1, p. 010201 (2023).

[14] M. Lewenstein, N. Baldelli, U. Bhattacharya, J. Biegert, M. F. Ciappina, U. Elu, T. Grass, P. T. Grochowski, A. Johnson, T. Lamprou, A. S. Maxwell, A. Ordóñez, E. Pisanty, J. Rivera-Dean, P. Stammer, I. Tyulnev and P. Tzallas, Attosecond physics and quantum information science, arXiv:2208.14769 [physics, physics:quant-ph] (2022).

[15] U. Bhattacharya, T. Lamprou, A. S. Maxwell, A. Ordóñez, E. Pisanty, J. Rivera-Dean, P. Stammer, M. F. Ciappina, M. Lewenstein and P. Tzallas, Strong–laser–field physics, non–classical light states and quantum information science, *Reports on Progress in Physics* **86**, 9, p. 094401 (2023).

[16] A. Pizzi, A. Gorlach, N. Rivera, A. Nunnenkamp and I. Kaminer, Light emission from strongly driven many-body systems, *Nature Physics* **19**, pp. 551–561 (2023).

[17] T. Lamprou, J. Rivera-Dean, P. Stammer, M. Lewenstein and P. Tzallas, Nonlinear optics using intense optical Schrödinger "cat" states, arXiv:2306.14480 [physics, physics:quant-ph] (2023).

[18] P. Stammer, J. Rivera-Dean, T. Lamprou, E. Pisanty, M. F. Ciappina, P. Tzallas and M. Lewenstein, High photon number entangled states and coherent state superposition from the extreme ultraviolet to the far infrared, *Physical Review Letters* **128**, 12, p. 123603 (2022).
[19] P. Stammer, Theory of entanglement and measurement in high-order harmonic generation, *Physical Review A* **106**, 5, p. L050402 (2022).
[20] J. Rivera-Dean, P. Stammer, A. S. Maxwell, T. Lamprou, P. Tzallas, M. Lewenstein and M. F. Ciappina, Light-matter entanglement after above-threshold ionization processes in atoms, *Physical Review A* **106**, 6, p. 063705 (2022).
[21] J. Rivera-Dean, P. Stammer, A. S. Maxwell, Th. Lamprou, E. Pisanty, P. Tzallas, M. Lewenstein, and M. F. Ciappina, Quantum-optical analysis of high-order harmonic generation in H_2^+ molecules, *Physical Review A* **109**, 3, p. 033706 (2024).
[22] P. Stammer and M. Lewenstein, Quantum optics as applied quantum electrodynamics is back in town, *Acta Physica Polonica A* **143**, 6, pp. S42–S42 (2023).
[23] P. Stammer, J. Rivera-Dean, A. S. Maxwell, T. Lamprou, J. Argüello-Luengo, P. Tzallas, M. F. Ciappina and M. Lewenstein, Entanglement and squeezing of the optical field modes in high harmonic generation, *Physical Review Letters* **132**, 14, p. 143603 (2024).
[24] M. Even Tzur, M. Birk, A. Gorlach, M. Krüger, I. Kaminer and O. Cohen, Photon-statistics force in ultrafast electron dynamics, *Nature Photonics* **17**, 6, pp. 501–509 (2023).
[25] Y. Fang, F.-X. Sun, Q. He and Y. Liu, Strong-field ionization of hydrogen atoms with quantum light, *Physical Review Letters* **130**, 25, p. 253201 (2023).
[26] M. E. Tzur and O. Cohen, Motion of charged particles in bright squeezed vacuum, *Light: Science & Applications* **13**, p. 41 (2024).
[27] A. Gorlach, M. E. Tzur, M. Birk, M. Krüger, N. Rivera, O. Cohen and I. Kaminer, High-harmonic generation driven by quantum light, *Nature Physics* **19**, pp. 1689–1696 (2023).
[28] P. Stammer, On the limitations of the semi-classical picture in high harmonic generation, arXiv:2308.15087 [physics, physics:quant-ph] (2023).
[29] P. Stammer, On the role of the optical phase and coherence in high harmonic generation, arXiv:2309.05010 [quant-ph] (2023).
[30] I. Gonoskov, R. Sondenheimer, C. Hünecke, D. Kartashov, U. Peschel and S. Gräfe, Nonclassical light generation and control from laser-driven semiconductor intraband excitations, *Physical Review B* **109**, 12, p. 125110 (2024).
[31] J. Rivera-Dean, P. Stammer, A. S. Maxwell, T. Lamprou, A. F. Ordóñez, E. Pisanty, P. Tzallas, M. Lewenstein and M. F. Ciappina, Entanglement and non-classical states of light in a strong-laser driven solid-state system, arXiv:2211.00033 [physics, physics:quant-ph] (2023).
[32] J. Rivera-Dean, P. Stammer, A. S. Maxwell, Th. Lamprou, A. F. Ordóñez, E. Pisanty, P. Tzallas, M. Lewenstein, and M. F. Ciappina, Nonclassical

states of light after high-harmonic generation in semiconductors: A Bloch-based perspective, *Physical Review B* **109**, 3, p. 035203 (2024).

[33] A. H. Chin, O. G. Calderón and J. Kono, Extreme midinfrared nonlinear optics in semiconductors, *Physical Review Letters* **86**, 15, pp. 3292–3295 (2001).

[34] S. Ghimire, A. D. DiChiara, E. Sistrunk, P. Agostini, L. F. DiMauro and D. A. Reis, Observation of high-order harmonic generation in a bulk crystal, *Nature Physics* **7**, 2, pp. 138–141 (2011).

[35] H. Haug and S. W. Koch, Periodic Lattice of Atoms, in *Quantum Theory of the Optical and Electronic Properties of Semiconductors* 4th Edition, World Scientific, pp. 41–44 (2004).

[36] G. Vampa, C. McDonald, G. Orlando, D. Klug, P. Corkum and T. Brabec, Theoretical analysis of high-harmonic generation in solids, *Physical Review Letters* **113**, 7, p. 073901 (2014).

[37] G. Vampa, C. R. McDonald, G. Orlando, P. B. Corkum and T. Brabec, Semiclassical analysis of high harmonic generation in bulk crystals, *Physical Review B* **91**, 6, p. 064302 (2015).

[38] E. N. Osika, A. Chacón, L. Ortmann, N. Suárez, J. A. Pérez-Hernández, B. Szafran, M. F. Ciappina, F. Sols, A. S. Landsman and M. Lewenstein, Wannier-Bloch approach to localization in high-harmonics generation in solids, *Physical Review X* **7**, 2, p. 021017 (2017).

[39] L. Li, P. Lan, X. Zhu and P. Lu, High harmonic generation in solids: particle and wave perspectives, *Reports on Progress in Physics* **86**, 11, p. 116401 (2023).

[40] L. Yue and M. B. Gaarde, Introduction to theory of high-harmonic generation in solids: tutorial, *JOSA B* **39**, 2, pp. 535–555 (2022).

[41] S. Jiang, J. Chen, H. Wei, C. Yu, R. Lu and C. Lin, Role of the transition dipole amplitude and phase on the generation of odd and even high-order harmonics in crystals, *Physical Review Letters* **120**, 25, p. 253201 (2018).

[42] J. L. Krause, K. J. Schafer and K. C. Kulander, High-order harmonic generation from atoms and ions in the high intensity regime, *Physical Review Letters* **68**, 24, pp. 3535–3538 (1992).

[43] P. B. Corkum, Plasma perspective on strong field multiphoton ionization, *Physical Review Letters* **71**, 13, pp. 1994–1997 (1993).

[44] K. C. Kulander, K. J. Schafer and J. L. Krause, Dynamics of Short-Pulse Excitation, Ionization and Harmonic Conversion, in B. Piraux, A. L'Huillier and K. Rzążewski (Eds.), Super-Intense Laser — Atom Physics. Springer, pp. 95–110 (1993).

[45] M. Lewenstein, P. Balcou, M. Y. Ivanov, A. L'Huillier and P. B. Corkum, Theory of high-harmonic generation by low-frequency laser fields, *Physical Review A* **49**, 3, pp. 2117–2132 (1994).

[46] F. Bloch, Über die Quantenmechanik der Elektronen in Kristallgittern, *Zeitschrift für Physik* **52**, 7, pp. 555–600 (1929).

[47] E. Goulielmakis and T. Brabec, High harmonic generation in condensed matter, *Nature Photonics* **16**, 6, pp. 411–421 (2022).

[48] P. C. Becker, H. L. Fragnito, C. H. B. Cruz, R. L. Fork, J. E. Cunningham, J. E. Henry and C. V. Shank, Femtosecond photon echoes from band-to-band transitions in GaAs, *Physical Review Letters* **61**, 14, pp. 1647–1649 (1988).

[49] M. T. Portella, J. Bigot, R. W. Schoenlein, J. E. Cunningham and C. V. Shank, k-space carrier dynamics in GaAs, *Applied Physics Letters* **60**, 17, pp. 2123–2125 (1992).

[50] I. Kilen, M. Kolesik, J. Hader, J. V. Moloney, U. Huttner, M. K. Hagen and S. W. Koch, Propagation induced dephasing in semiconductor high-harmonic generation, *Physical Review Letters* **125**, 8, p. 083901 (2020).

[51] M. Kolesik and J. V. Moloney, Numerical discreteness and dephasing in high-harmonic calculations in solids, *Physical Review B* **108**, 11, p. 115433 (2023).

[52] K. Amini, J. Biegert, F. Calegari, A. Chacón, M. F. Ciappina, A. Dauphin, D. K. Efimov, C. F. d. M. Faria, K. Giergiel, P. Gniewek, A. S. Landsman, M. Lesiuk, M. Mandrysz, A. S. Maxwell, R. Moszyński, L. Ortmann, J. A. Pérez-Hernández, A. Picón, E. Pisanty, J. Prauzner-Bechcicki, K. Sacha, N. Suárez, A. Zaïr, J. Zakrzewski and M. Lewenstein, Symphony on strong field approximation, *Reports on Progress in Physics* **82**, 11, p. 116001 (2019).

[53] W. Kohn, Analytic Properties of Bloch waves and Wannier functions, *Physical Review* **115**, 4, pp. 809–821 (1959).

[54] G. G. Brown, A. Jiménez-Galán, R. E. F. Silva and M. Ivanov, A real-space perspective on dephasing in solid-state high harmonic generation, arXiv:2210.16889 [cond-mat, physics:physics] (2022).

[55] M. O. Scully and M. S. Zubairy, Quantum Theory of Radiation, in *Quantum Optics*. Cambridge University Press, pp. 1–45 (2001).

[56] C. Gerry and P. Knight, Field Quantization, in *Introductory Quantum Optics*. Cambridge University Press, pp. 10–42 (2005).

[57] R. Loudon, Quantization of the Radiation Field, in *The Quantum Theory of Light*. Oxford University Press, pp. 125–179 (1973).

[58] W. Vogel and D.-G. Welsch, Elements of Quantum Electrodynamics, in *Quantum Optics*. John Wiley & Sons, pp. 15–72 (2006).

[59] R. J. Glauber, Photon correlations, *Physical Review Letters* **10**, 3, pp. 84–86 (1963).

[60] R. J. Glauber, Coherent and incoherent states of the radiation field, *Physical Review* **131**, 6, pp. 2766–2788 (1963).

[61] R. J. Glauber, The quantum theory of optical coherence, *Physical Review* **130**, 6, pp. 2529–2539 (1963).

[62] E. Wigner, On the quantum correction for thermodynamic equilibrium, *Physical Review* **40**, 5, pp. 749–759 (1932).

[63] W. P. Schleich, Wigner Function, in *Quantum Optics in Phase Space*. John Wiley & Sons, pp. 67–98 (2001).

[64] R. L. Hudson, When is the Wigner quasi-probability density non-negative? *Reports on Mathematical Physics* **6**, 2, pp. 249–252 (1974).

[65] D. T. Smithey, M. Beck, M. G. Raymer and A. Faridani, Measurement of the Wigner distribution and the density matrix of a light mode using optical

homodyne tomography: Application to squeezed states and the vacuum, *Physical Review Letters* **70**, 9, pp. 1244–1247 (1993).

[66] A. Royer, Wigner function as the expectation value of a parity operator, *Physical Review A* **15**, 2, pp. 449–450 (1977).

[67] M. A. Nielsen and I. L. Chuang, Introduction to Quantum Mechanics, in *Quantum Computation and Quantum Information: 10th Anniversary Edition*. Cambridge University Press, pp. 60–119 (2010).

[68] L. Gurvits, Classical complexity and quantum entanglement, *Journal of Computer and System Sciences* **69**, 3, pp. 448–484 (2004).

[69] M. A. Nielsen and I. L. Chuang, Entropy and Information, in *Quantum Computation and Quantum Information: 10th Anniversary Edition*. Cambridge University Press, pp. 500–527 (2010).

[70] M. B. Plenio and S. Virmani, An introduction to entanglement measures, *Quantum Information & Computation* **7**, 1, pp. 1–51 (2007).

[71] C. H. Bennett and G. Brassard, Quantum cryptography: Public key distribution and coin tossing, *Theoretical Computer Science* **560**, pp. 7–11 (2014).

[72] A. K. Ekert, Quantum cryptography based on Bell's theorem, *Physical Review Letters* **67**, 6, pp. 661–663 (1991).

[73] L. K. Grover, A fast quantum mechanical algorithm for database search, in *Proceedings of the Twenty-Eighth Annual ACM Symposium on Theory of Computing*, STOC '96. Association for Computing Machinery, pp. 212–219 (1996).

[74] P. W. Shor, Polynomial-time algorithms for prime factorization and discrete logarithms on a quantum computer, *SIAM Review* **41**, 2, pp. 303–332 (1999).

[75] M. D. Reid, P. D. Drummond, W. P. Bowen, E. G. Cavalcanti, P. K. Lam, H. A. Bachor, U. L. Andersen and G. Leuchs, Colloquium: The Einstein-Podolsky-Rosen paradox: From concepts to applications, *Reviews of Modern Physics* **81**, 4, pp. 1727–1751 (2009).

[76] G. Wang and T.-Y. Du, Quantum decoherence in high-order harmonic generation from solids, *Physical Review A* **103**, 6, p. 063109 (2021).

[77] B. Sundaram and P. W. Milonni, High-order harmonic generation: Simplified model and relevance of single-atom theories to experiment, *Physical Review A* **41**, 11, pp. 6571–6573 (1990).

[78] N. Tsatrafyllis, I. K. Kominis, I. A. Gonoskov and P. Tzallas, High-order harmonics measured by the photon statistics of the infrared driving-field exiting the atomic medium, *Nature Communications* **8**, 1, p. 15170 (2017).

[79] N. Tsatrafyllis, S. Kühn, M. Dumergue, P. Foldi, S. Kahaly, E. Cormier, I. Gonoskov, B. Kiss, K. Varju, S. Varro and P. Tzallas, Quantum optical signatures in a strong laser pulse after interaction with semiconductors, *Physical Review Letters* **122**, 19, p. 193602 (2019).

[80] G. Ndabashimiye, S. Ghimire, M. Wu, D. A. Browne, K. J. Schafer, M. B. Gaarde and D. A. Reis, Solid-state harmonics beyond the atomic limit, *Nature* **534**, 7608, pp. 520–523 (2016).